7-1-2016

TEMPERATURE DEPENDENT THERMOELECTRIC CHARACTERIZATION OF ORGANIC MATERIALS

Mohammad Abir Hossain

Mohammad Abir Hossain
Candidate

Mechanical Engineering
Department

This thesis is approved, and it is acceptable in quality and form for publication:

Approved by the Thesis Committee:

Dr. Mehran Tehrani, Chairperson

Dr. Yu-Lin Shen

Dr. Zayd Leseman

TEMPERATURE DEPENDENT THERMOELECTRIC CHARACTERIZATION OF ORGANIC MATERIALS

BY

MOHAMMAD ABIR HOSSAIN

BACHELOR OF SCIENCE IN MECHANICAL ENGINEERING
BANGLADESH UNIVERSITY OF ENGINEERING AND TECHNOLOGY
FEBRUARY 2011

THESIS

Submitted in Partial Fulfillment of the
Requirements for the Degree of

Master of Science in Mechanical Engineering

The University of New Mexico
Albuquerque, New Mexico

July 2016

DEDICATION

This thesis is dedicated to my lovely and caring wife for her continuous support throughout my journey at UNM. Without her support and sacrifices, it would have been difficult to reach my goal. I also want to thank my parents for their care and inspiration that helped me to pursue my dreams.

ACKNOWLEDGEMENT

I would like to thank my adviser, Prof. Mehran Tehrani, for his guidance and support throughout this thesis work. He has been an inspirational mentor, and helped me with intricate suggestions that motivated me to complete the project. Besides, he has been a really good friend who maintained a comfortable and approachable work environment that helped me a lot as an international student.

TEMPERATURE DEPENDENT THERMOELECTRIC CHARACTERIZATION OF ORGANIC MATERIALS

By

Mohammad Abir Hossain

B.S., Mechanical Engineering, Bangladesh University of Engineering and Technology, 2011

M.S., Mechanical Engineering, The University of New Mexico, 2016

ABSTRACT

Thermoelectric energy conversion represents a solid-state technology based on the "Seebeck phenomenon", where a temperature gradient generates an electrical voltage difference across semiconductors. Conversely, cooling (refrigeration) can be achieved by applying an electric voltage across the material. One can imagine countless opportunities where thermoelectrics could be used for cooling or harvesting heat to produce energy. Recently, thermoelectric energy conversion has received a great deal of attention as a promising technology to generate electricity from waste heat. Much effort has been put into the improvement and/or development of thermoelectric materials, both inorganic and organic, with higher power conversion efficiency. Organic materials and specifically carbon nanotube (CNT) based thermoelectrics have recently shown great promise for thermoelectric applications. The most efficient organic thermoelectric materials reported to date have efficiencies that are comparable to that of bismuth telluride at room temperature, which has the highest reported *ZT* for a bulk inorganic material at room temperature (*ZT*~1). Although the potential of organic thermoelectrics is clear, there is

insufficient fundamental information to provide a clear path to the optimization of their performance. Thermoelectric conversion efficiency is accompanied by a high electrical conductivity, high Seebeck coefficient and a low thermal conductivity. Organic thermoelectric materials have an inherent low thermal conductivity. Researchers have therefore focused on the improvement of the Seebeck coefficient and electrical conductivity of these materials. On the experimental front, it is crucial to establish processing-thermoelectric properties-structure relationships for organic materials. There are no set standards, methods or setups for measuring the characteristic properties of thermoelectrics, i.e., Seebeck coefficient, electrical conductivity and thermal conductivity. In this thesis, the design and development of a novel apparatus for the simultaneous measurement of electrical resistivity and Seebeck coefficient of films is reported. Sample mount, where the sample is placed with all connections for measurement and data acquisition, is integrated inside a cryostat chamber enabling measurements over the 10-400 K temperature range. This temperature range is suitable for organic thermoelectrics in that it captures their performance in their intended application environment (i.e., 200-400 K) and provides insight on their structure and transport mechanisms (10-300 K). The whole setup is automated and computer controlled via LabVIEW, for measurement and data acquisition. The program executes all the steps to run the experiment, acquires the measured values, and executes calculations to provide Seebeck coefficient and electrical conductivity as a function of temperature. The sample holder is plug and play type that can be easily mounted or dismounted from the sample stage or sample mount inside the cryostat chamber. Finite element method was used to analyze the thermo-mechanical response of the sample holder in the 10-400 K range. The

apparatus was calibrated against high purity Nickel film and a very good agreement was found. Lastly, spray coated polymer and carbon nanotube-based films were characterized using this device. The analysis of these results revealed the different transport mechanisms in these systems.

TABLE OF CONTENTS

LIST OF FIGURES x

LIST OF TABLES xiii

CHAPTER 1: INTRODUCTION 1

1.1 Background 1

1.2 Thermoelectric Materials 3

1.3 Measurement Devices 4

1.4 Thermoelectric Characterization of Polymers at 10–400 K 11

1.5 Design Considerations 12

CHAPTER 2: DESIGN OF THE ROOM TEMPERATURE CHARACTERIZATION APPARATUS 14

2.1 Working Principle 14

2.2 Room Temperature Seebeck Measurement Setup 14

2.3 Room Temperature Electrical Resistivity Measurement Setup 17

2.4 Device Calibration 19

2.5 Validation and Results 23

CHAPTER 3: DESIGN OF THE CRYOGENIC CHARACTERIZATION APPARATUS 27

3.1 Cryogenic Vacuum Chamber 27

3.2 Sample Holder 29

3.3 Temperature Measurement and Control 32

3.4 Electrical Resistivity Measurement 33

3.5 Seebeck Coefficient Measurement 34

3.6 Measurement and Data Acquisition with LabVIEW 37

3.7 Validation and Results 38

CHAPTER 4: FINITE ELEMENT MODELING 41

4.1 FEM Model 41

4.2 Temperature Distribution 43

4.3 Thermal Stresses 45

4.4 Convergence Study 46

CHAPTER 5: ORGANIC SAMPLE CHARACTERIZATION 47

5.1 Conducting Polymer for Organic Thermoelectrics 47

5.2 Sample Preparation 49
5.3 Seebeck Coefficient and Electrical Resistivity Results..... 52
CHAPTER 6: CONCLUSION AND FUTURE WORK 58
APPENDIX..... 60
REFERENCES..... 66

LIST OF FIGURES

Figure 1. Schematic of (a) the Peltier and (b) the Seebeck effects. [1] 2

Figure 2. Schematic of: (a) the cross sectional view of the sample mount. C1 and C2 are the coil heaters in boron nitride blocks and (b) the top view of the sample mount. T1 and T2 are thermocouples, and P1 and P2 are tungsten probes.[16] 6

Figure 3. Schematic of the temperature and voltage measurement device used by G-H Kim et al. [4] 7

Figure 4. Schematic diagrams of the measurement setup used by Rajeev Singh et al.[11] .. 8

Figure 5. (a) Circuit diagram of the high-speed transient measurement system with packaged device circuit (b) Circuit diagram of in-plane Seebeck voltage measurement showing four quantities measured from type R thermocouples in real time. [11] 9

Figure 6. Placement of thermocouples for Seebeck coefficient measurement: (a) use of thermocouple to measure both temperature and Seebeck voltage; (b) arrangement of thermocouple wires; (c) basic Seebeck coefficient measurement geometry. [12] 10

Figure 7. Different arrangement of placing the thermocouple for Seebeck coefficient measurement as described by Iwanaga et al. [12] 11

Figure 8. SolidWorks model of the experimental setup for room temperature Seebeck measurement: (a) front view; (b) isometric view. 15

Figure 9. Room temperature Seebeck measurement setup. 16

Figure 10. Seebeck measurement setup showing the placement of sample and probes. . 16

Figure 11. Experimental setup for electrical resistivity measurement: (a) top view; (b) isometric view. 17

Figure 12. Picture of actual setup for electrical resistivity measurement: (a) electrical connection to instruments; (b) placement of a copper sample on the device; (c) placement of top support; (d) sample is clamped and ready for measurement. 18

Figure 13. Seebeck Calibration plots for Al, Ni and Mo. 22

Figure 14. Illustrative plot of Seebeck validation results compared to reported values in literature. 24

Figure 15. Illustrative plot of electrical resistivity validation results compared to reported values in literature. 25

Figure 16. Advanced research system (ARS) Cryostat or cryogenic vacuum chamber. . 28

Figure 17. Cryogenic vacuum chamber accessories: (a) compressor, (b) cooling unit, and (c) vacuum pump. 28

Figure 18. SolidWorks design of the sample holder: (a) and (b) dismantled device showing different components and arrangements; (c) top view; (d) front view; (e) sample holder after assembly. 30

Figure 19. Different views of the actual sample holder and sample mount: (a) sample holder without the top supports and a sample showing the measurement probes, (b) bottom side of the sample holder showing the pins for plugging into the mount; (c) sample mount inside the cryostat; (d) sample holder plugged into the sample mount with a sample in place. 31

Figure 20. Thermopower or Seebeck coefficient of pure copper as a function of temperature. Solid line represents the interpolation function; hollow circles represent data from Roberts [44]; squares from Burkov et al. [17]; triangles from Cusack and Kendall [41]; diamonds from MacDonald [43] and Blatt [45]; and filled circles from Gold et al. [42] 36

Figure 21. Measurement and data acquisition devices: DC Precision Current Source, Nanovoltmeter, Temperature Controller and Computer with the LabVIEW program. 37

Figure 22. Electrical resistivity of nickel measured using the cryogenic device and compared to previously reported data. Squares represent the data from Burkov et al. [17], pluses from White and Woods [46], crosses from Laubitz et al. [36], and circles represent the experimental data. Inset is the magnified plot over the 10-50 K range. 39

Figure 23. Absolute Seeebck coefficient of nickel compared to previously reported data. Blue and green triangles are from Blatt et al. [47] for unannealed and annealed Ni, respectively; squares from Boffoue et al. [15]; diamonds from Beretta et al. [19]; pluses from Burkov et al. [17]; hollow circles from Laubitz et al. [36]; and filled circles are the results of this study. 40

Figure 24. Finite element model of the sample holder after meshing. 42

Figure 25. Direction of input heat flux: (a) sample holder and sample mount dismantled, showing the direction of heat flux; (b) dismantled view from the right hand side; (c) sample mount and holder connected together. 43

Figure 26. Temperature distribution across the sample holder when cooled down from room temperature to 10 K in 50 mins. 44

Figure 27. Equivalent von-Mises stress across the copper parts of the sample holder. 45

Figure 28. Mesh convergence study of the FEM simulation 46

Figure 29. Representative organic thin film sample for characterization in 10-400 K: (a) showing the gold coating for thermal and electrical contact; (b) flexible thin film on PET substrate. 51

Figure 30. Organic thin film samples for characterization at room temperature: (a) sample for electrical conductivity measurement showing the silver strips for electrical contact; (b) sample for Seebeck coefficient measurement showing silver dots for good thermal and electrical contact. 52

Figure 31. Seebeck coefficient of different organic samples at room temperature. 53

Figure 32. Electrical conductivity of different organic samples at room temperature. ... 54

Figure 33. Electrical resistivity of the 5vol% EG mixed PEDOT:PSS sample in the 10-400 K temperature range..... 55

Figure 34. Seebeck coefficient of the 5vol% EG mixed PEDOT:PSS sample in the 10-400 K temperature range..... 55

Figure 35. Electrical resistivity of the DWCNT-PEDOT:PSS sample in the 10-400 K temperature range..... 56

Figure 36. Seebeck coefficient of the DWCNT-PEDOT:PSS sample in the 10-400 K temperature range..... 57

Figure 37. Block diagram (flow chart) of the experimental control and data acquisition process..... 60

Figure 38. Front panel of the main VI of the LabVIEW program. 61

Figure 39. Block diagram of the main VI of the LabVIEW program. The red boxes shows the SubVIs:(a) SubVI to read temperature data from 4 RTD sensors; (b) SubVI for electrical resistivity measurement; (c) SubVI for Seebeck coefficient measurement. 62

Figure 40. SubVI for electrical resistivity measurement. 63

Figure 41. SubVI for Seebeck coefficient measurement. Red boxes represent: (a) SubVI to configure heater parameters; (b) SubVI to read temperature data from 4 RTD sensors. 64

Figure 42. SubVI to read temperature data from 4 RTD sensors. 65

Figure 43. SubVI to read data from single RTD sensor..... 65

Figure 44. SubVI to configure heater parameters. 65

LIST OF TABLES

Table 1. Validation results for Seebeck coefficient measurement (without silver paste). 23

Table 2. Validation results for Seebeck coefficient measurement (with silver paste). 24

Table 3. Validation results for electrical resistivity measurements. 25

CHAPTER 1: INTRODUCTION

1.1 Background

The generation of electricity from thermal energy, by applying a temperature gradient across two dissimilar materials, was discovered by Thomas Johann Seebeck in 1822. The phenomenon is called the Seebeck effect. In 1834, Jean Charles Athanase Peltier demonstrated that heat can be pumped by applying electric current (Peltier effect), a phenomenon with great potential for refrigeration. Later around 1850s, Lord Kelvin explained the physics of the Seebeck and Peltier effects attributing that the reversible heat flow discovered by Peltier must have entropy associated with it, and the Seebeck coefficient was a measure of the entropy associated with the electric current. Thermoelectric is the technology used for power generation and active cooling, based on the principles of the Seebeck and Peltier effect respectively. The efficiency of the thermoelectric power generation process was derived in 1911 by Edmund Altenkirch. (Reference: [1])

In many respects, thermoelectric generators (TEGs) show advantages compared to conventional power sources in that they are solid state devices with no moving parts, silent and vibration-free, highly reliable, and robust. For many years TEGs have, however, been restricted to niche applications such as power supplies for space missions such as the “Voyager”. With increasing efficiency of the thermoelectric materials and reduced production cost, thermoelectric devices may eventually be heading for important breakthroughs. Today, although expensive, the first wrist-watches powered by body-heat that are working on the thermoelectric principle are commercially available.

To understand the thermoelectric effect, we need to consider two materials in a thermocouple connected between a hot reservoir (T_h) and a cold reservoir (T_c).

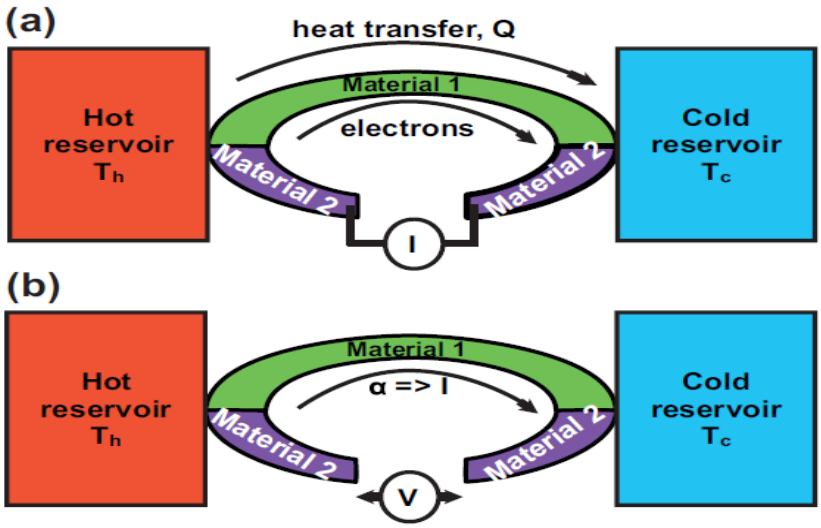

Figure 1. *Schematic of (a) the Peltier and (b) the Seebeck effects.* [1]

As shown in Figure 1(a), when a current is applied across material 2, heat is pumped from the hot reservoir to the cold reservoir. The Peltier coefficient, π, for this system is given by

$$\pi = \frac{Q}{I} \tag{1}$$

where Q is the pumped heat and I is the applied current. The unit of π is Volt and the Peltier coefficient is the heat energy carried by each electron per unit charge and time from the hot reservoir to the cold reservoir.

The Seebeck effect requires a similar arrangement, but the gap in material two is electrically disconnected (Figure 1(b)). When there is a temperature difference between the material junctions, an open circuit voltage (ΔV) is generated which is proportional to

($T_h - T_c$) = ΔT. The constant of proportionality is called the Seebeck coefficient, *S*. More generally the Seebeck coefficient is defined as

$$S = -\frac{\Delta V}{\Delta T} \tag{2}$$

The unit of Seebeck coefficient is Volts per Kelvin. The Seebeck coefficient is *1/q* times the entropy (*Q/T*) transported with each electron, where *q* is the electron charge. Hence, the Peltier effect is just each electron in the electrical current transferring an amount of heat from one reservoir to the other i.e., a heat pump.

1.2 Thermoelectric Materials

Nearly 58% of the total energy generated in the U.S. in 2012 was rejected into the environment, mostly in the form of low-grade waste heat, i.e., 40-200 °C.[2] Development of thermoelectric materials that efficiently convert this low-grade waste heat into usable energy will be extremely beneficial to meet the energy needs of today's society.[3] The few inorganic thermoelectric candidates for this temperature range suffer from high fabrication cost, usage of rare earth or toxic elements, or poor mechanical properties. Organic materials are particularly an attractive alternative in that they are cheap, abundant, non-toxic, flexible, and can be produced using scalable processes. Moreover, recent developments [4,5] in organic thermoelectric materials and their synthesis techniques show potential means to increase their efficiency, also known as the figure of merit. The figure of merit of the thermoelectric materials is a dimensionless parameter expressed as,

$$ZT = \frac{S^2\sigma}{\kappa}T \tag{3}$$

where *S* is the Seebeck coefficient, σ is the electrical conductivity, κ is the thermal conductivity and *T* is the absolute temperature in kelvins. One of the main constraints

towards the efficiency improvement is that the thermal conductivity, electrical conductivity and thermopower are interdependent. There are certain tradeoffs among these parameters that make it difficult to maximize one parameter without affecting the others. C. Yu et al.[6] reported a nanocomposite containing single wall carbon nanotubes, PEDOT:PSS [poly(3,4-ethylenedioxythiophene): poly(styrenesulfonate)] and/or polyvinyl acetate (PVA) that has weak correlation between thermopower and electrical conductivity resulting in large thermoelectric power factor ($S^2\sigma$) of 160 μW/mK^2 at room temperature, with a high electrical conductivity of 1000 S/cm. Recent development has showed a *ZT* value of 0.42 for PEDOT:PSS at room temperature.[7] Texas A&M researchers have achieved power factors ($S^2\sigma$) of 2700 μW/mK^2 for a layer by layer assembly of carbon nanotube and Graphene nanocomposite.[8] This value is comparable to the power factor of Bismuth Telluride at room temperature. Organic or polymeric conducting materials have an inherently low thermal conductivity, which is very desirable for thermoelectric materials. The focus in organic thermoelectrics is therefore on optimizing the power factor.

1.3 Measurement Devices

There are many reports on devices and methods for measuring the thermopower and/or electrical conductivity of thermoelectric materials over different temperature ranges from cryogenic to very high temperatures.[9-21] There are also reports on the direct measurement of *ZT*.[9,10,11] Many of these studies are focused on characterizing the thermopower of bulk inorganic materials,[12,13,14] from room to high temperatures, mainly due to the intended application environment. However, there has been a few reports on

thermoelectric characterization apparatuses for films or thin films,[11,15,16,17,18] in particular organic thin films.[19,20] In order to search for or develop efficient thermoelectrics, it is crucial to develop measurement devices that enable facile and relatively fast monitoring of electrical resistivity and Seebeck coefficient of organic samples over their service temperatures. Moreover, cryogenic studies of the electrical resistivity and Seebeck coefficient can shed light on transport mechanisms in organic materials. To serve these two purposes, 10-400 K temperature range was chosen for this apparatus. There are few reports of low temperature characterization of organic materials,[15,21] however, the author is not aware of any reports on a single apparatus for characterization of thermoelectric films and bulk materials from 10 to 400 K.

Ravichandran et al.[16] developed a device that can simultaneously measure the electrical conductivity and thermopower of thin film samples in the temperature range of 300K to 750K. They used DC differential and van der Pauw methods for the measurements of thermopower and electrical conductivity, respectively. The schematic of their device is provided in figure 2(a) and 2(b). Their setup consists of a sample mount placed inside a vacuum chamber. The sample mount was thermally isolated from the base plate by a zirconia standoff (low thermal conductivity), which helped to achieve high temperature at the sample mount. A radiation shield made of stainless steel was used to reduce radiation losses. The sample mount had a base heater, and a thin inconel plate with two boron nitride blocks on the top that housed the coil heaters. Use of high power heaters and a base heater helped to reach high temperatures and large temperature gradients. Temperature of the boron nitride blocks were controlled through a PID loop

controlled by a Eurotherm 2416. The position of boron nitride blocks could be adjusted using fastening screws allowing the use of different sized samples.

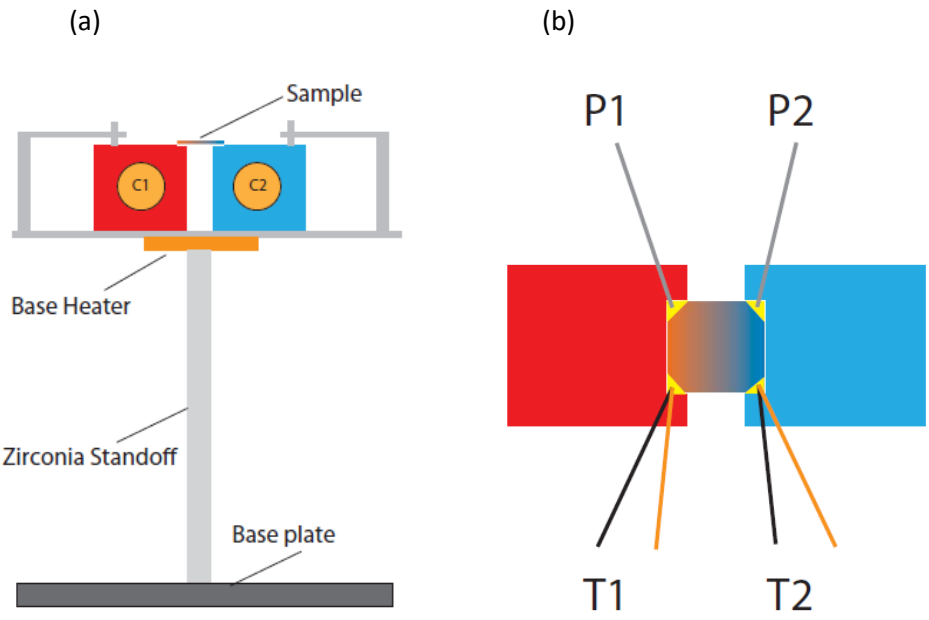

Figure 2. *Schematic of: (a) the cross sectional view of the sample mount. C1 and C2 are the coil heaters in boron nitride blocks and (b) the top view of the sample mount. T1 and T2 are thermocouples, and P1 and P2 are tungsten probes.*[16]

Two K-type thermocouples were used for temperature measurements across the boron nitride blocks and two tungsten probes were connected to the other two corners of the sample. The alumel lead of the thermocouples was used to measure the thermoelectric voltage. Same lead wires (chromel and alumel) were used for the thermocouple wires in order to avoid spurious thermoelectric voltage between the lead wires and the thermocouple wires. The thermocouples were thermally anchored to the sample using silver paint. Agilent 34970A switch with built-in digital multimeter was used for thermopower measurements. Keithley 6220 current source and 2182A nanovoltmeter, in conjunction with the switch, were used for van der Pauw electrical conductivity

measurements. The apparatus was computer controlled with a LabVIEW program for measurement and data acquisition.

Kim et al.[4] reported on a device that can be used for the characterization of doped organic semiconductors. The schematic of their measurement setup is provided in Figure 3 where they characterized a PEDOT:PSS thin film sample on glass substrate. For the Seebeck and electrical conductivity measurements, gold electrode pairs were deposited on the surface of PEDOT:PSS at different spacing. The deposited metal contact dimensions were 1.2x1.5 mm. The four probe method was used to measure the electrical conductivity for each electrode spacing.

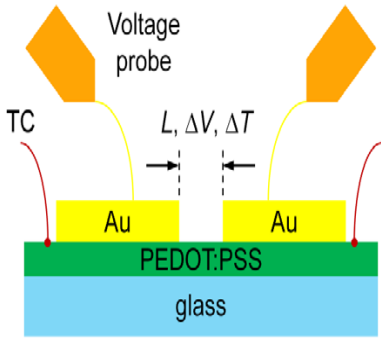

Figure 3. *Schematic of the temperature and voltage measurement device used by G-H Kim et al.* [4]

A Peltier cooler (300 K - ΔT_0) and a Peltier heater (300 K + ΔT_0) were used to apply a temperature gradient. Two micro-thermocouples (TCs) of 25 µm diameter were placed on the sample to the outer sides of the gold electrodes (as depicted in Figure 3) with a separation of D, which was much larger than the TC diameter, the electrode spacing (L), and the error in TC position. The temperature difference between the TCs (ΔT_{TC}) was measured for different values of D (1, 2, 3, 4, and 5 mm) and showed a linear temperature gradient variation ($\Delta T_{TC}/D$ = constant). Since ΔT_{TC} and D were much larger than their

corresponding errors, the error in the derived temperature gradient was small. The temperature differences across the electrode spacing (ΔT) were derived as $\Delta T = \Delta T_{TC} \times L/D$. To measure the thermal voltage, two thin gold wires of 25 µm diameter were brought into contact with the gold electrodes. Thermal voltage (ΔV) was found to increase linearly with the electrode spacing. The Seebeck coefficient was derived using a linear fit to the measured ΔV versus ΔT data at different electrode spacing.

Singh et al.[11] designed and fabricated a device for thermoelectric characterization of thin films from room temperature to 850 K. The schematic of the measurement setup is provided in Figure 4.

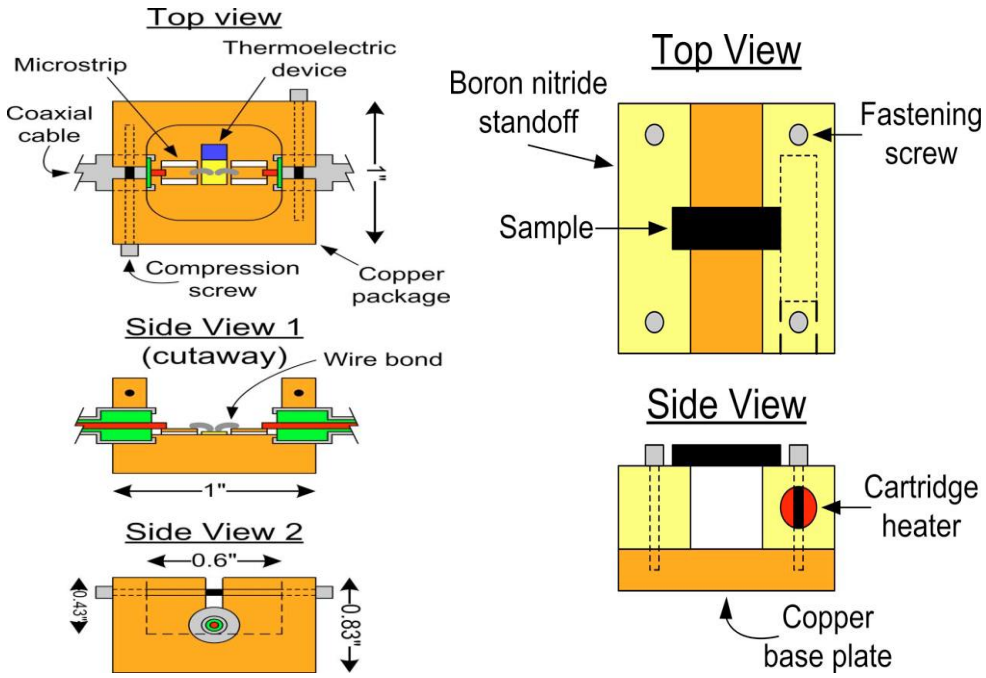

Figure 4. *Schematic diagrams of the measurement setup used by Rajeev Singh et al.*[11]

In their setup the sample was placed across two boron nitride stands, and a temperature gradient was created across the sample by a heater embedded in one of the standoffs. . Two thermocouples were placed at the edges of sample and were used to measure

temperature and voltage difference. The measurement circuit is shown in Figure 5(a & b). Four HP 34420A nanovoltmeters were used to read the temperatures and the Seebeck voltage generated in the sample. The relative Seebeck coefficient of the sample was measured relative to platinum or type *R* thermocouple leads.

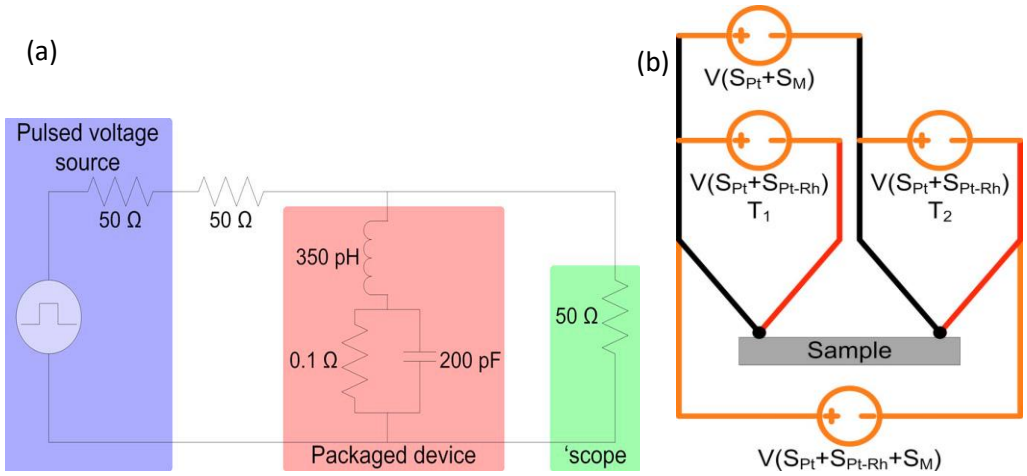

Figure 5. *(a) Circuit diagram of the high-speed transient measurement system with packaged device circuit (b) Circuit diagram of in-plane Seebeck voltage measurement showing four quantities measured from type R thermocouples in real time.* [11]

They assumed the thin junction between the two leads to be isothermal. Random noise in the system was reported to be ±200 nV in Seebeck voltage and ±30 mK in temperature difference. Measurement of in-plane resistivity was carried out using the van der Pauw technique. Two thermocouple probes were used in conjunction with two platinum probes to source current and measure voltage in various sample configurations. Pulsed current of low duty cycle was used in measurements to minimize the effect of sample Seebeck voltage on the measured resistivity measurements. The voltage response is measured with an oscilloscope, which allowed the observation of potential Seebeck voltage transients affecting the measurement.

Iwanaga et al.[12] reported a high temperature apparatus (room-1200 K) for the measurement of Seebeck coefficient using uniaxial 4-point contact geometry. They also reviewed different design geometries (Figure 7) for such measurements and discussed major design considerations. As shown in Figure 6(a), two probes make point contacts with the material and serve as both thermocouples and voltage leads. Figure 6(b) shows the arrangement of thermocouple wires having point contact with the sample. Figure 6(c) represents a basic Seebeck coefficient measurement setup with an elongated geometry. The assumptions for such a measurement are: (a) the system is in steady state during the measurement of the temperature and voltage, and that both measurements occur simultaneously, (b) the voltage response to the temperature gradient is linear, and (c) the measurement of temperature and voltage occurs at the same point on the sample. Though in a real setup, these assumptions are hard to achieve and non-negligible errors are often present.

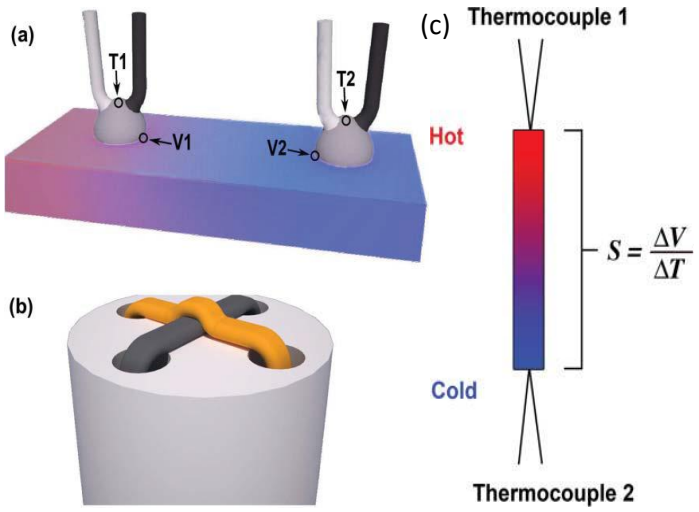

Figure 6. *Placement of thermocouples for Seebeck coefficient measurement: (a) use of thermocouple to measure both temperature and Seebeck voltage; (b) arrangement of thermocouple wires; (c) basic Seebeck coefficient measurement geometry.* [12]

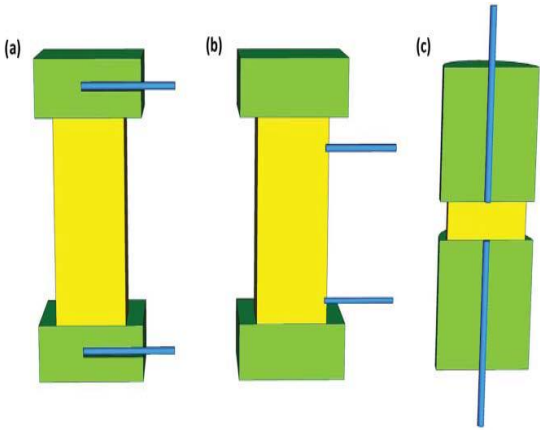

Figure 7. *Different arrangement of placing the thermocouple for Seebeck coefficient measurement as described by Iwanaga et al.* [12]

1.4 Thermoelectric Characterization of Polymers at 10–400 K

Organic materials are particularly an attractive alternative in that they are cheap, abundant, safe, and can be produced using scalable processes (e.g., roll-to-roll (R2R)). Organic and specifically carbon nanotube (CNT) based thermoelectrics have recently shown great promise for thermoelectric applications.[22]

Advancements in thermoelectrics over the last two decades have been achieved mainly through creating materials with defined nanoscale structures and interfaces. The science that relates these structures to thermoelectric performance (structure-property relationships) has been central to the development of efficient inorganic materials. For organic thermoelectrics, however, an Edisonian approach has thus far been sought; mainly due to the lack of the relevant fundamental science. Theoretical studies predict *ZT* values in excess of 2 for CNT samples and over 10 in semiconducting CNT assemblies;[23, 24] a *ZT* of 1 or higher is required for the commercialization of thermoelectric materials.[25] To verify the aforementioned theoretical studies, ultrahigh purity CNT samples of certain chiralities that are aligned in one direction are required. In practice, CNT-polymer

systems have exhibited vast potential for flexible thermoelectrics with power factors ($S^2\sigma$) as high as 500 μW/mK^2.[26-30] To put this in perspective, assuming a thermal conductivity of ~0.5 W/m/K, which is typical for such systems, current CNT-based thermoelectrics achieve a *ZT* of 0.3 at room temperature.

1.5 Design Considerations

In general, there are certain factors to keep in mind when designing a thermoelectric characterization apparatus suitable for 10-400 K range: (1) the device must operate in vacuum; any air or moisture in the chamber will condense on the sample at cryogenic temperatures, leading to erroneous measurements. Also, vacuum reduces the noise in data and eliminates convective heat losses, (2) temperature and voltage measurements should be simultaneous and corrected for any offset such as the Seebeck of the probes, (3) probes should have very good thermal and electrical contact with the sample surface. It is very important to assure Ohmic contacts for electrical measurements, (4) when using separate probes for temperature and voltage measurements, distance between them should be very small for accurate Seebeck measurement, (5) electrical isolation of the entire sample is required for resistivity measurements, (6) sample holder should possess temperature compatibility, chemical inertness and electrical isolation, (7) a radiation shield is required around the sample holder to minimize the irradiation effects, (8) connections and lead wires should be of the same material to avoid spurious thermoelectric voltage at junctions. A novel setup for the simultaneous measurement of the in-plane thermopower and electrical resistivity of thin film and bulk samples from 10 to 400 K was designed and realized. Separate resistance temperature detector (RTD) and

voltage (Cu wire) sensors for thermopower measurements were used.[31] Unlike thermocouples, there is no need for an ice bath or reference point for cold junction compensation when using small RTDs as temperature sensors. With one less temperature measurement (of the ice bath or reference point), the uncertainty of the measurements decreases. Besides, RTDs are more robust and offer a better accuracy, stability and repeatability. The flat surface of the RTD prevents film puncture under pressure contacts. All the probes in this design were individually spring mounted to ensure good thermal and electrical contacts to the sample. Using the spring mount, the need for any additional bonding material [13,14,16] between the sensors and the sample was eliminated, and the setup allowed to repeat measurements on a sample. It is desirable to induce smaller temperature gradients (ΔT) for differential thermopower measurements.[31] Many devices, however, do not use small temperature differences, i.e., < 1K. [12,15,17,20,21] In the presented apparatus, ΔT was always less than 1 K, ensuring negligible changes in measurement parameters (i.e., thermopower of reference probes), and therefore a much higher accuracy can be realized. The apparatus also enables heating the sample from either side, thus canceling the spurious thermal electromotive force (emf) produced in the electrical circuit. Lastly, the sample holder in this design can be readily plugged and unplugged from the cold head of the cryo-chamber.

CHAPTER 2: DESIGN OF THE ROOM TEMPERATURE CHARACTERIZATION APPARATUS

2.1 Working Principle

Design, development and calibration of an apparatus for room temperature measurement of the Seebeck coefficient and electrical resistivity of film samples are presented in this chapter. Two separate devices for the measurement of these parameters were built. For the Seebeck coefficient measurement, sample was heated from one side to produce an in-plane temperature gradient, generating a voltage difference across the sample. Subsequently, temperature and voltage differences along the specimen length were measured. The ratio between the induced voltage and the temperature difference is defined as the Seebeck coefficient. For electrical resistivity measurement, the traditional four point DC measurement was carried out.

2.2 Room Temperature Seebeck Measurement Setup

The schematic of the experimental setup is shown in Figures 8, 9 and 10. Typical size of samples was 15x20 mm. Two rectangular copper pieces with through holes were used as the heating block and heat sink. A cylindrical cartridge heater (Thorlabs, Model HT15W) was placed inside the heating block. The sample was placed horizontally on the copper blocks (Figure 10). Two K type thermocouples (Omega Engineering) made contact with the sample close to the copper blocks and measured the temperatures of the hot and the cold sides of sample. Two vertical voltage probes were placed parallel and adjacent to the thermocouples to measure the voltage difference across the sample. As shown in Figure 8, all probes were spring mounted to ensure good contact and uniform

force distribution on sample. The block, holding the four tubes with voltage and temperature probes inside was screw-driven.

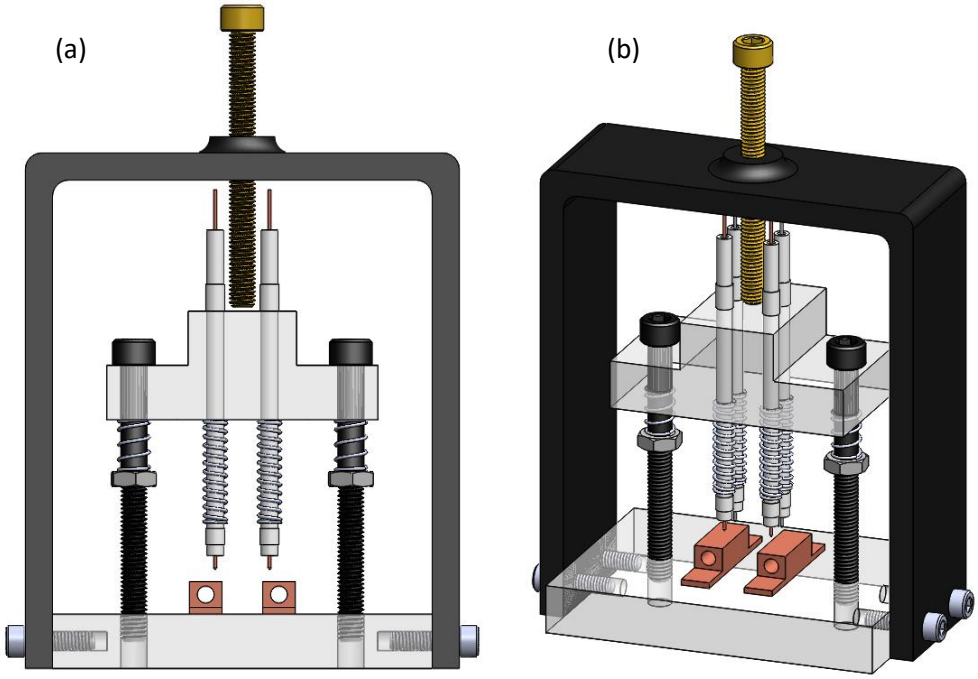

Figure 8. *SolidWorks model of the experimental setup for room temperature Seebeck measurement: (a) front view; (b) isometric view.*

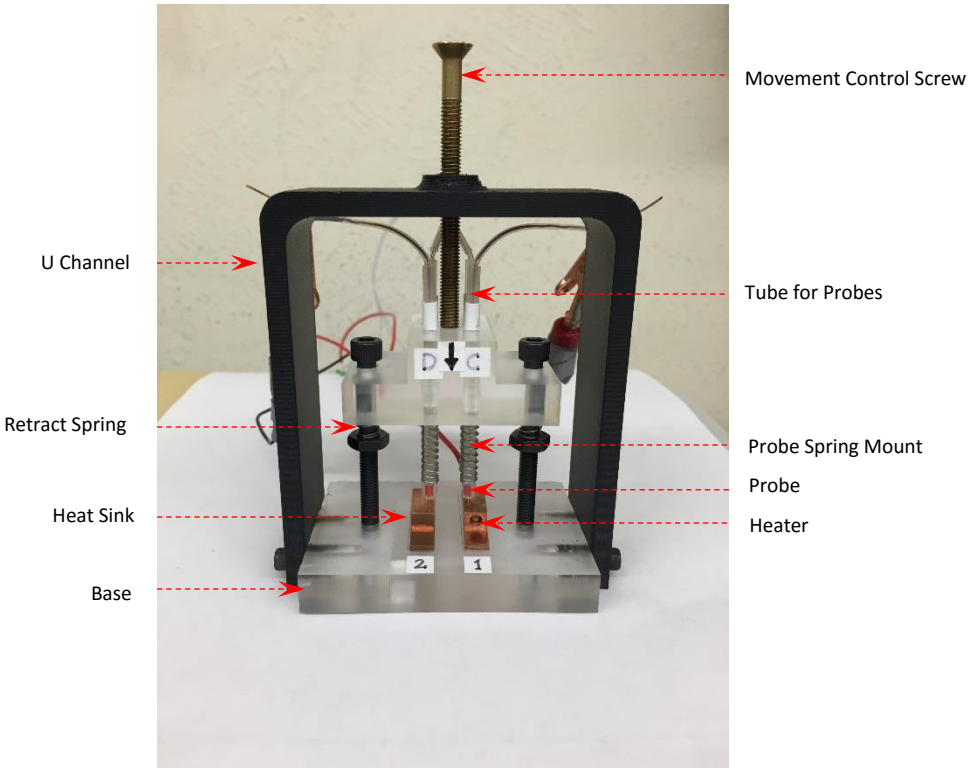

Figure 9. *Room temperature Seebeck measurement setup.*

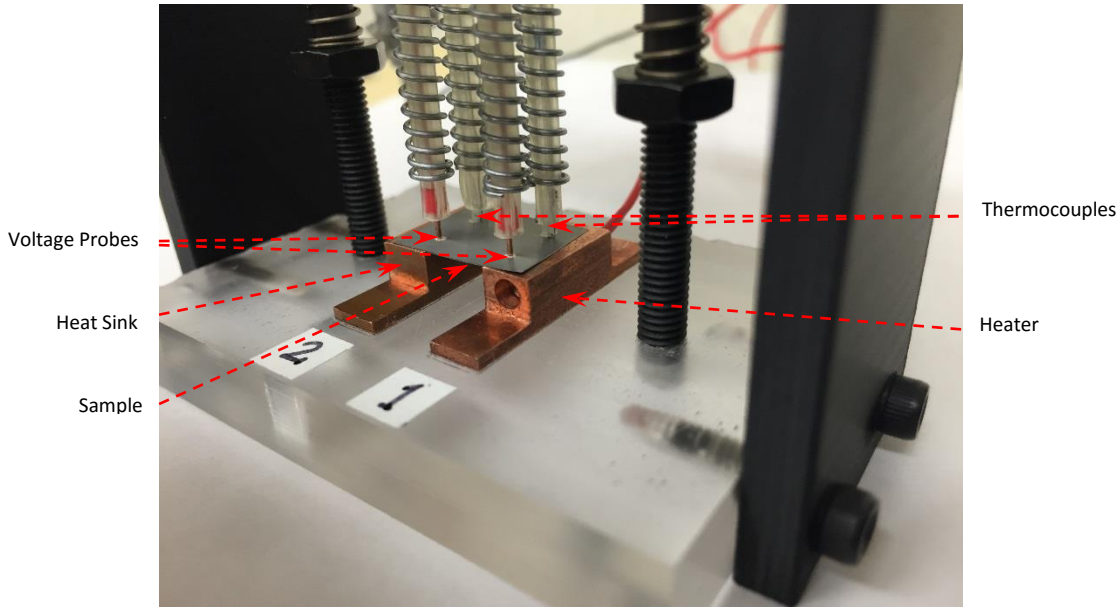

Figure 10. *Seebeck measurement setup showing the placement of sample and probes.*

The two screws were spring loaded to facilitate the retraction of the probes. The U channel housed the movement control screw that was used for vertical movement of the

probes and to apply an even pressure on the probes (Figure 9). The whole setup sat on a polyethylene block for good thermal and electrical isolation. A nanovoltmeter (Keithley Instruments, Model: 2182A) and a temperature controller (LakeShore Cryotonics, Model: 336) were used for voltage measurement and temperature measurement/control, respectively. The setup was interfaced with a computer via LabVIEW. LabVIEW was used for data acquisition and controlling the experiments.

2.3 Room Temperature Electrical Resistivity Measurement Setup

DC four-point method was used for electrical resistivity measurements at room temperature. As shown in Figures 11 and 12, the setup consisted of four thin copper wires on an electrically insulating acrylic glass substrate. The outer two wires were used to supply the current from a dc current source (Keithley 6221 DC and AC Current Source). The inner two wires were used to sense the voltage drop across the sample, and were connected to a nanovoltmeter (Keithley 2182A Nanovoltmeter).

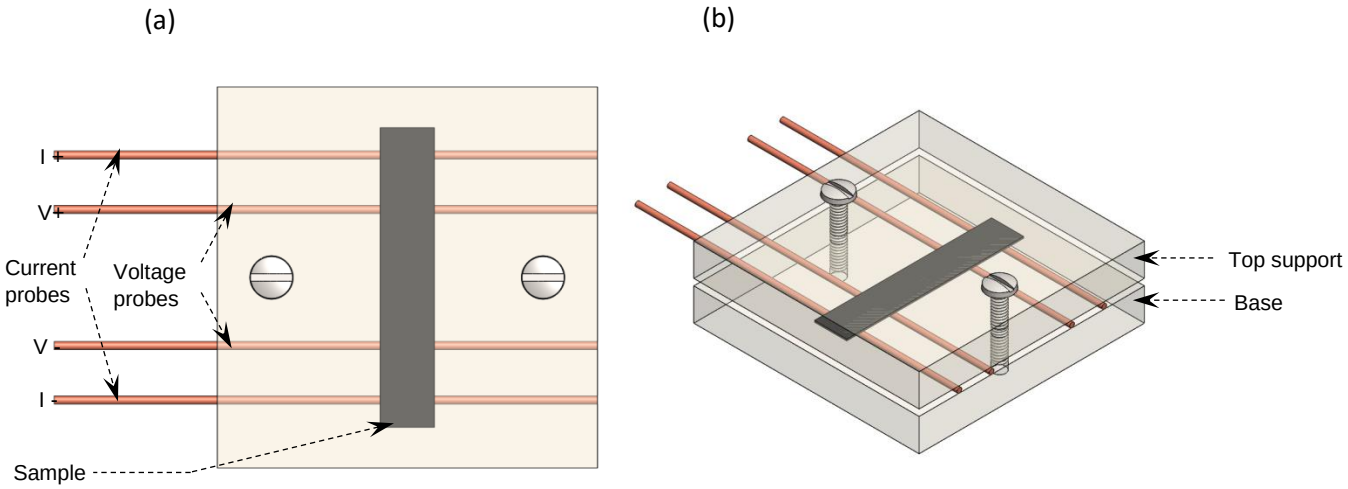

Figure 11. *Experimental setup for electrical resistivity measurement: (a) top view; (b) isometric view.*

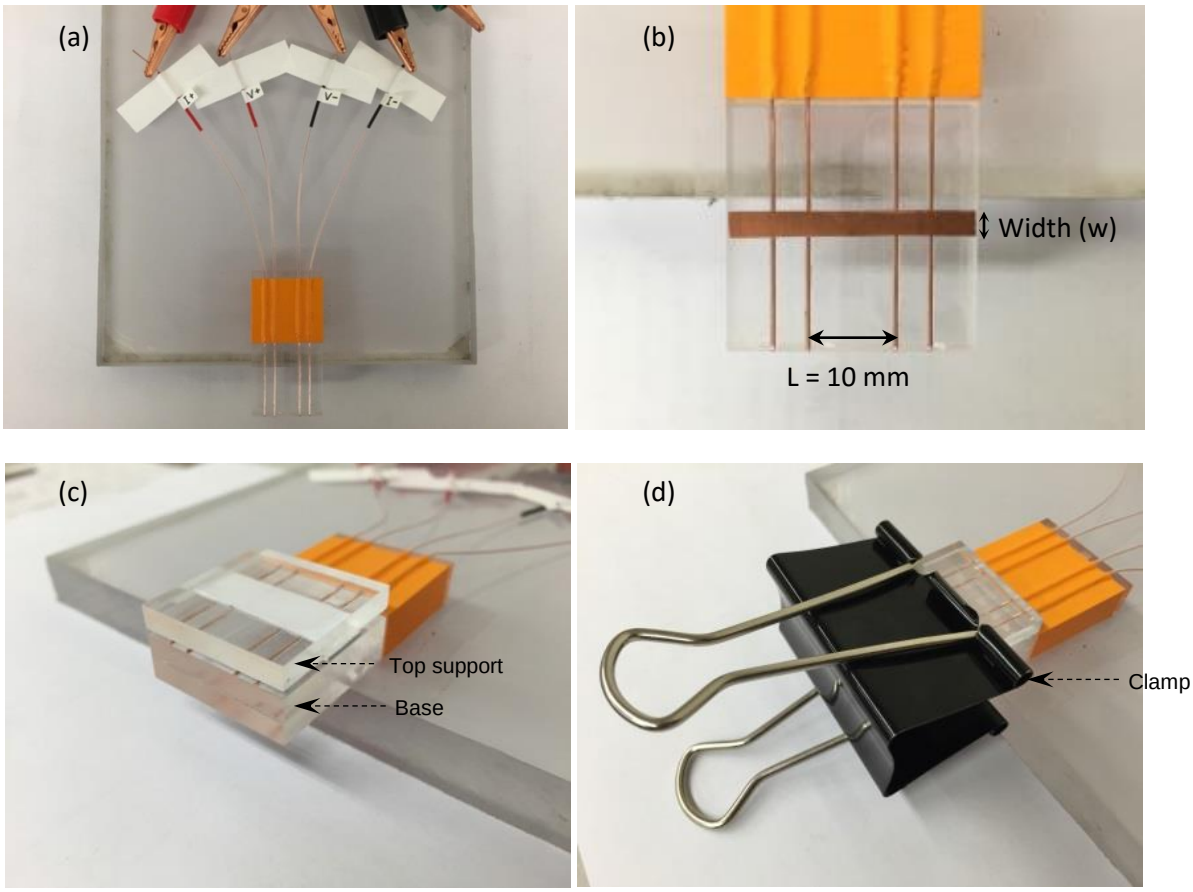

Figure 12. *Picture of actual setup for electrical resistivity measurement: (a) electrical connection to instruments; (b) placement of a copper sample on the device; (c) placement of top support; (d) sample is clamped and ready for measurement.*

Another acrylic sheet was used to hold the sample against the copper wires for uniform contact and pressure. This part was attached to the base with two screws. Under this arrangement, small and constant current pulses (<0.1 A) with reversing polarity were sent through the cross section of the sample and the voltages were measured at two intermediate points along the length using the voltage probes. This is a special combined mode (delta mode) operation of the Keithley 6221 current source and Keithley 2182A nanovoltmeter. The small reversing current pulses prohibit any resistive heating in thin samples and eliminate spurious Seebeck voltage that may cause measurement errors. The electrical resistivity is then calculated using the relation

$$\rho = \frac{\frac{V}{I} \times w \times t}{L} \quad (4)$$

where ρ is the electrical resistivity, V is the measured voltage, I is the supplied current, w is the sample width, t is sample thickness, and L is the length between the voltage probes or contacts. Several voltage readings were averaged when calculating the electrical resistivity.

2.4 Device Calibration

Three metal foil samples of aluminum, molybdenum and nickel (Advent Research Materials Ltd., UK) were used for the calibration. Copper was also used for the electrical resistivity calibration. The samples had a rectangular geometry (20x20 mm) with a thickness of 50 μm (except for Ni that was 125 μm). Aluminum, copper and nickel were 99.99% pure and molybdenum was 99.95% pure. Measurements were carried out both on bare samples and using small amount of silver on the 4 contact points. Seebeck voltages as a function of temperature difference for all samples with and without silver contacts are plotted in figure 13.

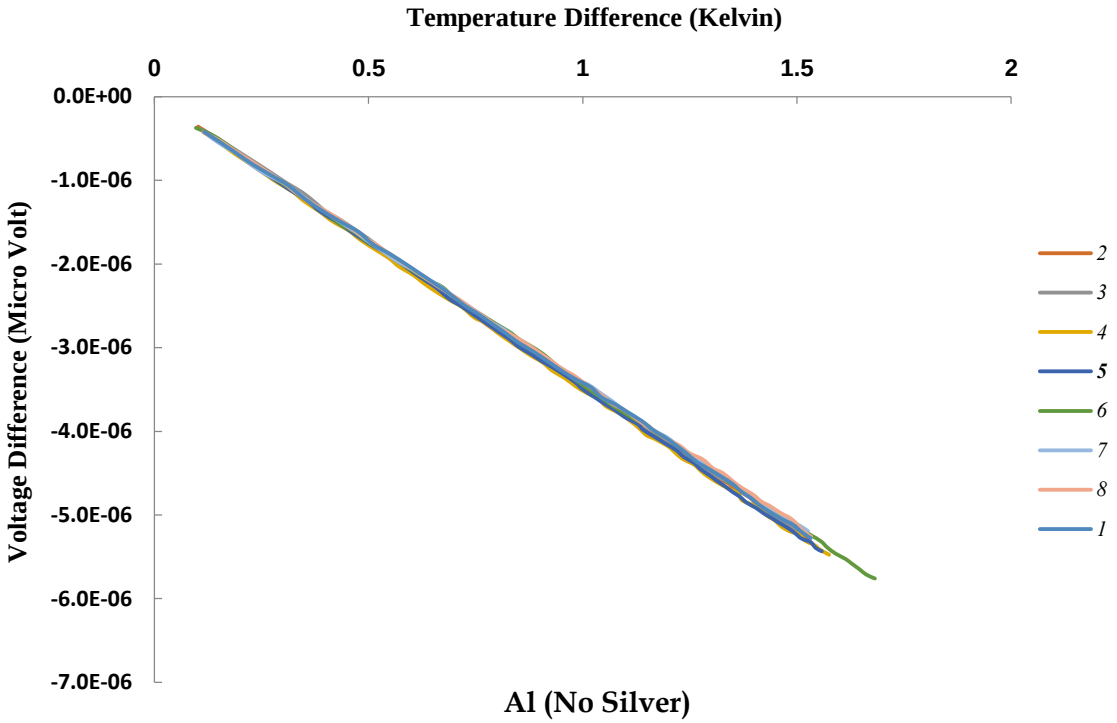
Temperature Difference (Kelvin)
0
0.5
1
1.5
2
0.0E+00
-1.0E-06
-2.0E-06
-3.0E-06
-4.0E-06
-5.0E-06
-6.0E-06
-7.0E-06
Voltage Difference (Micro Volt)
2
3
4
5
6
7
8
1
Al (No Silver)

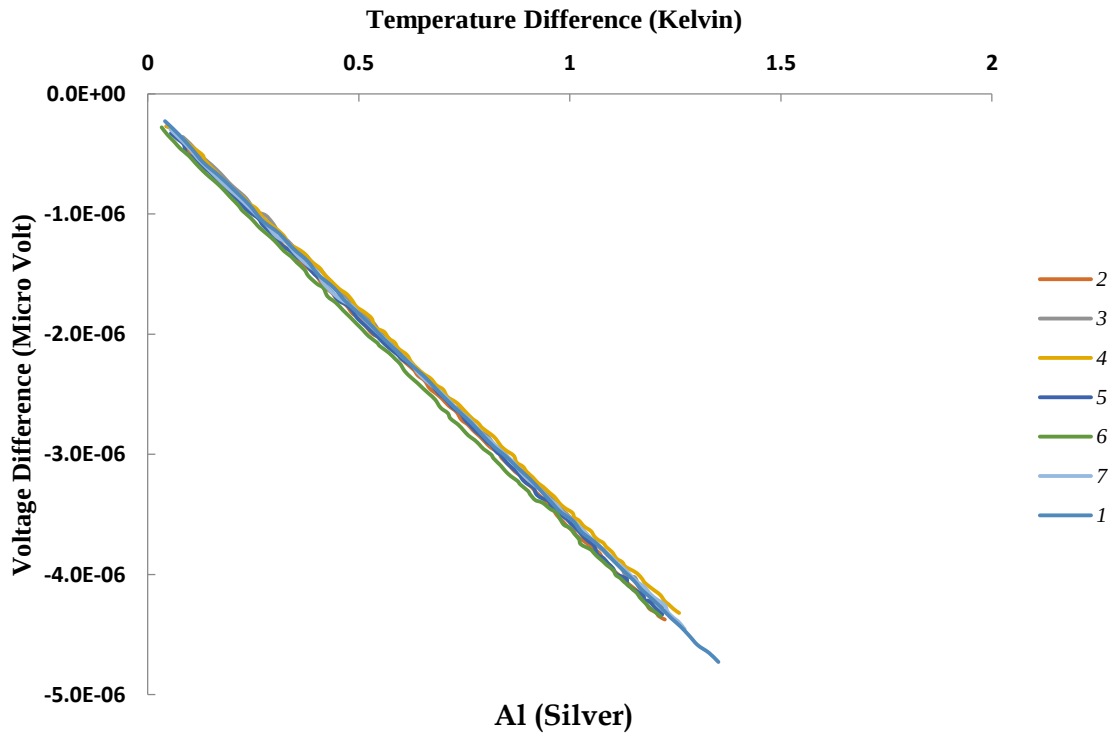
Temperature Difference (Kelvin)
0
0.5
1
1.5
2
0.0E+00
-1.0E-06
-2.0E-06
-3.0E-06
-4.0E-06
-5.0E-06
Voltage Difference (Micro Volt)
2
3
4
5
6
7
1
Al (Silver)

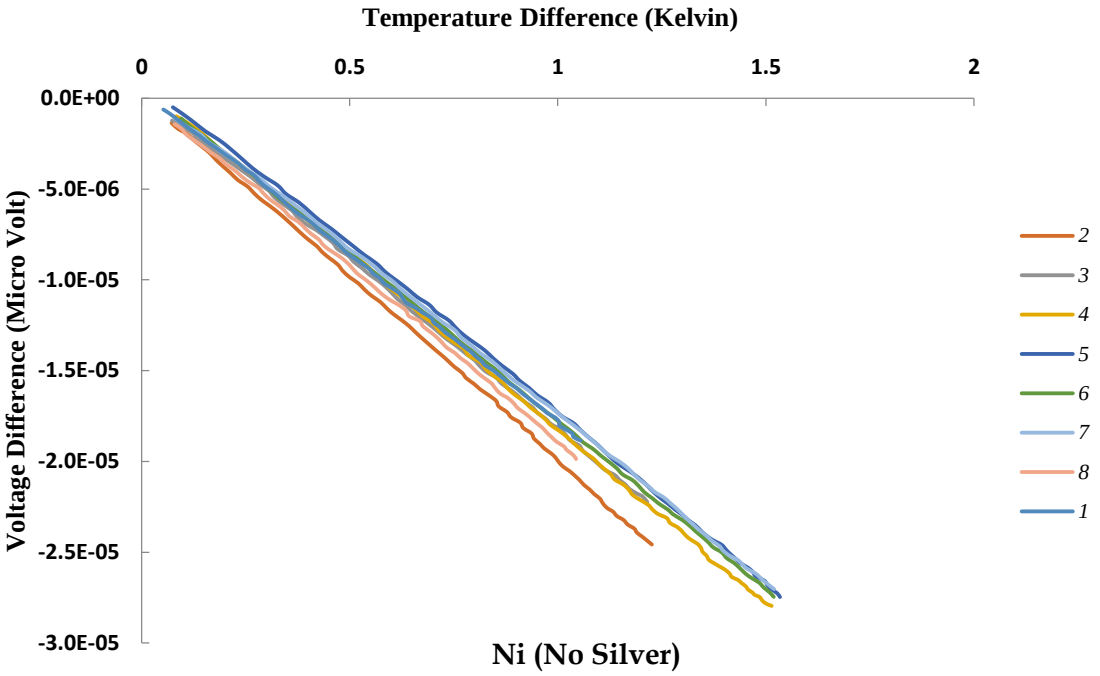
Temperature Difference (Kelvin)
0
0.5
1
1.5
2
0.0E+00
-5.0E-06
-1.0E-05
-1.5E-05
-2.0E-05
-2.5E-05
-3.0E-05
Voltage Difference (Micro Volt)
2
3
4
5
6
7
8
1
Ni (No Silver)

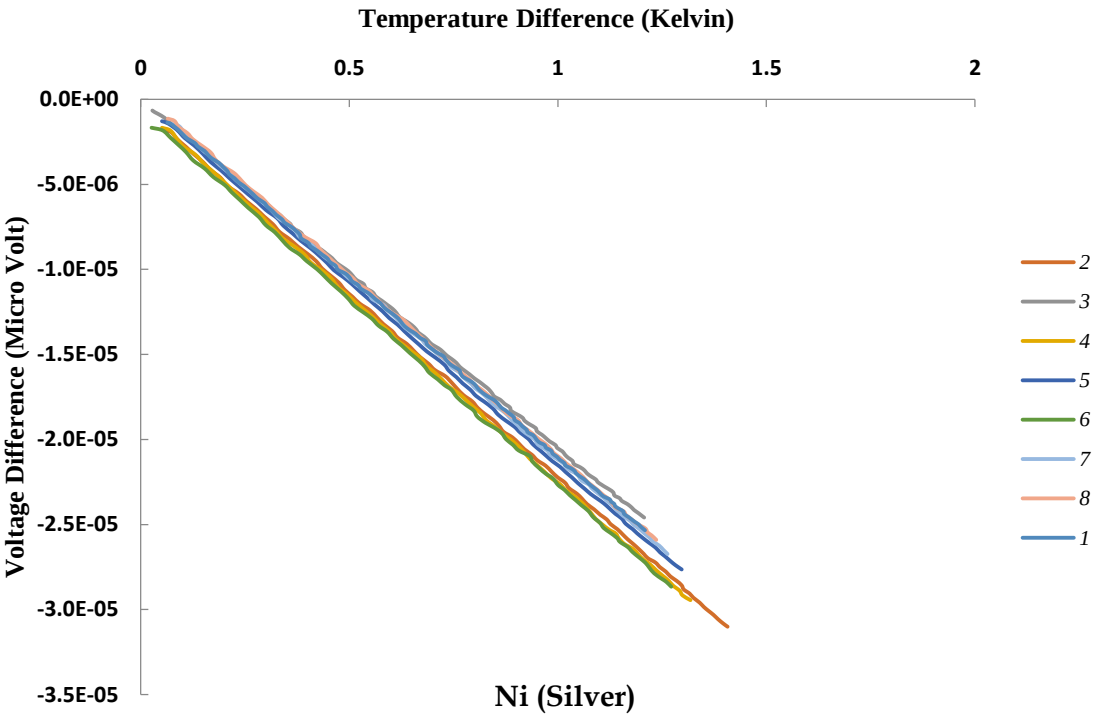
Temperature Difference (Kelvin)
0
0.5
1
1.5
2
0.0E+00
-5.0E-06
-1.0E-05
-1.5E-05
-2.0E-05
-2.5E-05
-3.0E-05
-3.5E-05
Voltage Difference (Micro Volt)
2
3
4
5
6
7
8
1
Ni (Silver)

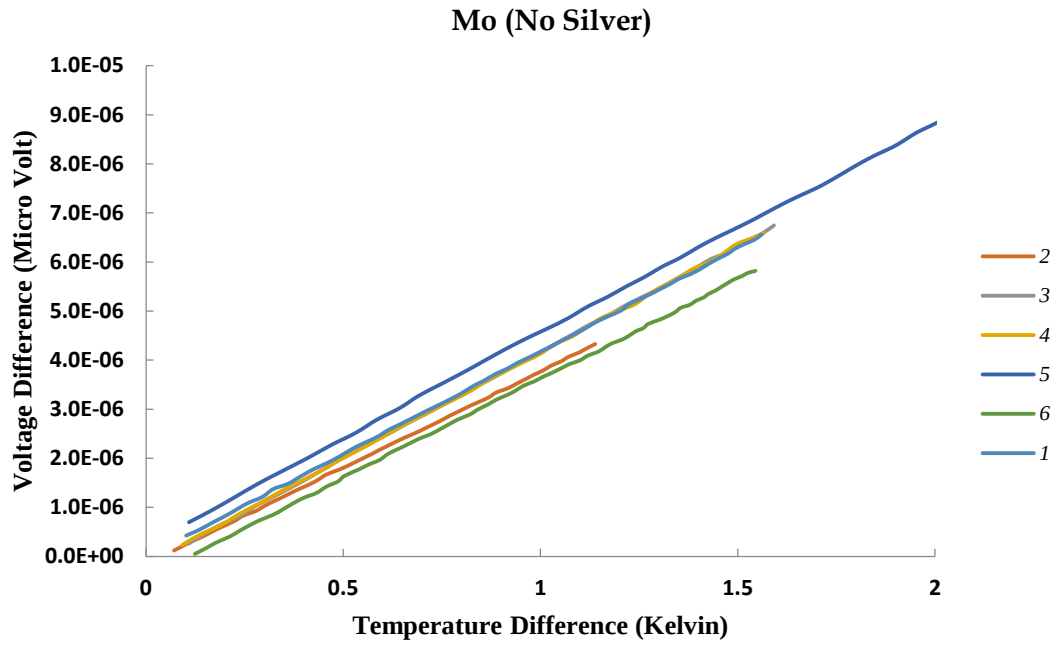

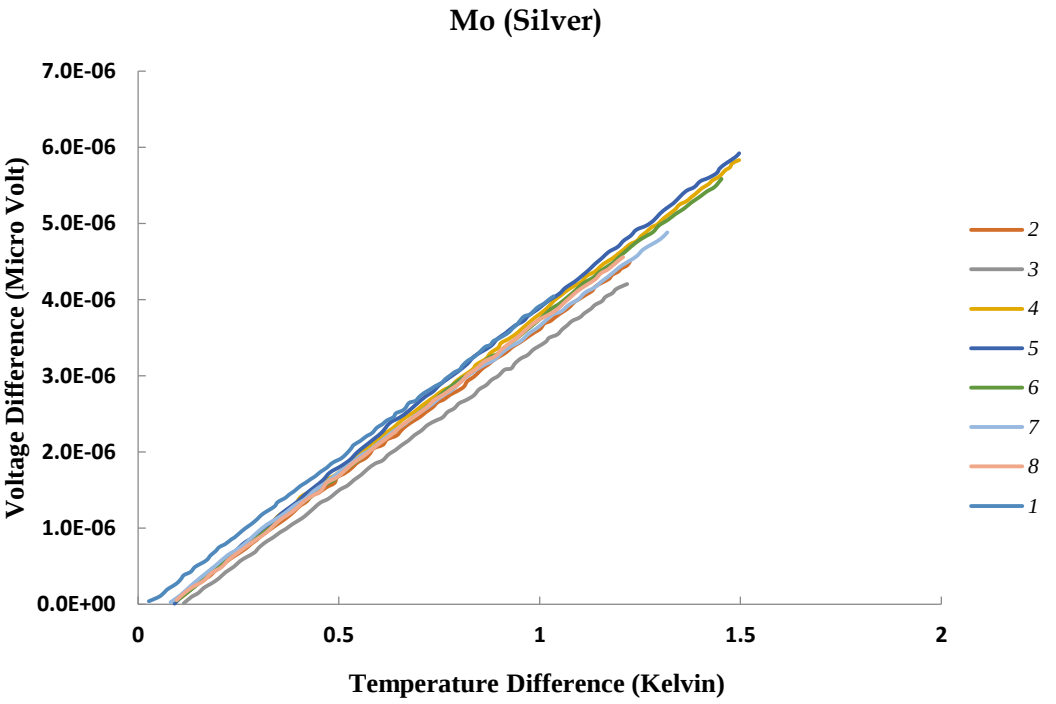

Figure 13. *Seebeck Calibration plots for Al, Ni and Mo.*

2.5 Validation and Results

All the validation results are provided in Tables 1, 2 and 3. Illustrative results are provided in Figures 14 and 15. From the Seebeck results in Table 1 and 2, we observed improvement (i.e., closer to literature values) in measured values when using the silver paste to make Ohmic contact with the probes. The Seebeck coefficient of Al was measured to be -1.62 μV/K. Ali Shakouri et al.[32] reported a value of -1.66 μV/K for Al. Ronald J. Gripshover et al.[33] reported the value to be -1.69 μV/K at 300 K. The experimental results agreed well with the reported Seebeck coefficient of Al. Also a Seebeck coefficient of 5.81 μV/K was measured for Mo, which is in good agreement to the reported value of 5.57 μV/K by S. O. Kasap [34] and 5.79 μV/K by J. P. Moore et al.[35] For Ni, the measured Seebeck coefficient using silver paint at the contact points was -19.56 μV/K. This is in very good agreement with the previously reported values [19,15,36].

Table 1. *Validation results for Seebeck coefficient measurement (without silver paste).*

Sample	**Seebeck Coefficient, S (μV/K)** [Without Silver contacts]							
	Test 1	Test 2	Test 3	Test 4	Test 5	Average Measured Value	Literature Value [Ref]	% Deviation from Literature
Aluminum (Al)	-1.59	-1.61	-1.63	-1.55	-1.63	**-1.60**	-1.66 [32]	3.49
Nickel (Ni)	-16.60	-16.80	-17.30	-16.80	-17.30	**-16.96**	-19.44 [36]	12.74
Molybdenum (Mo)	6.03	5.89	6.12	6.16	5.76	**5.99**	5.79 [35]	3.51

Table 2. *Validation results for Seebeck coefficient measurement (with silver paste).*

Sample	**Seebeck Coefficient, S (µV/K)** [With Silver contacts]							
	Test 1	Test 2	Test 3	Test 4	Test 5	Average Measured Value	Literature Value [Ref]	% Deviation from Literature
Aluminum (Al)	-1.65	-1.60	-1.59	-1.62	-1.63	**-1.62**	-1.66 [32]	2.53
Nickel (Ni)	-19.30	-19.40	-19.50	-20.10	-19.50	**-19.56**	-19.44 [36]	0.64
Molybdenum (Mo)	5.83	5.90	5.74	5.92	5.65	**5.81**	5.79 [35]	0.32

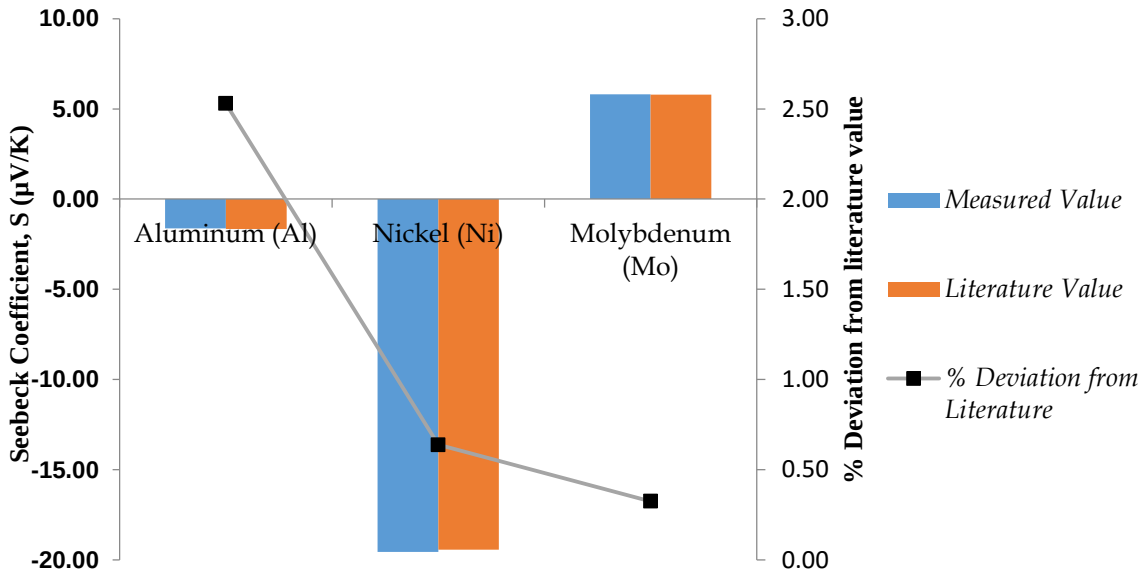

Figure 14. *Illustrative plot of Seebeck validation results compared to reported values in literature.*

The electrical resistivity results are provided in Table 3 and Figure 15. All the results are in good agreement with the previously reported values. The highest deviation from literature was found to be 6.81% for copper.

Table 3. *Validation results for electrical resistivity measurements.*

Sample	Electrical Resistivity, ρ (μΩ-cm)							
	Test 1	Test 2	Test 3	Test 4	Test 5	Average Measured Value	Literature Value [Ref]	% Deviation from Literature Value
Aluminum (Al)	2.81	2.81	2.82	2.81	2.82	**2.81**	2.73 [37]	2.97
Nickel (Ni)	7.35	7.36	7.36	7.36	7.38	**7.36**	7.24 [38]	1.74
Molybdenum (Mo)	5.86	5.86	5.92	5.85	5.85	**5.87**	5.52 [39]	6.34
Copper (Cu)	1.84	1.84	1.84	1.84	1.85	**1.84**	1.73 [40]	6.81

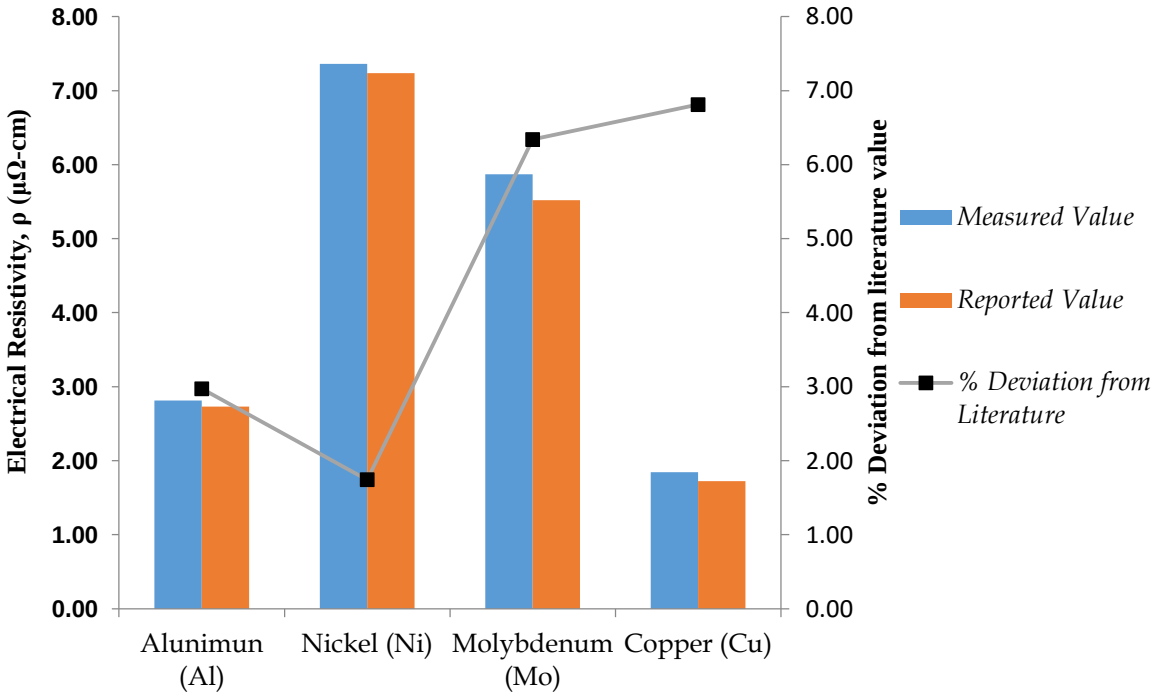

Figure 15. *Illustrative plot of electrical resistivity validation results compared to reported values in literature.*

From the dV/dT graphs of Seebeck coefficient measurements, a perfect linear relationship between the voltage (ΔV) and temperature difference (ΔT) is found that ensures the reliability of the measurements. Moreover, the small deviation in the

measurement results proves the repeatability of our apparatus. It is important to note that the slight deviation in Seebeck measurement may come from the 0.01% impurity in the samples. We induced a temperature gradient of 1-2 °C ($\Delta T \leq 2$ °C) so that the measurement parameters (i.e., Seebeck coefficient of reference probe) do not change much during a single measurement. This way we have increased the accuracy of our measurements. Furthermore, it is very important to ensure Ohmic contact between the sample and the probes to eliminate any contact resistance at the interface. For this, silver paint was used which improved the results appreciably.

For the electrical resistivity measurements, errors may arise from the dimensional measurements of the sample (i.e., thickness, width and length between voltage probes) and due to non-uniform contact between the sample and probes. By carefully measuring the dimensional parameters and pressing the sample against the probes, we have tried to eliminate or reduce such errors.

CHAPTER 3: DESIGN OF THE CRYOGENIC CHARACTERIZATION APPARATUS

3.1 Cryogenic Vacuum Chamber

Sample holder was placed inside a closed-cycle Helium cryogenic vacuum chamber (Advanced Research System, Model DE-202A) (Figure 16). An Adixen (Model Pascal 2005SD) vacuum pump was used to create vacuum inside the chamber (Figure 17(c)). Figure 17(a) shows the compressor (Advanced Research System, Model ARS-2HW) that was used to circulate Helium inside the chamber through a closed loop system to bring down the temperature of the cold head, also referred to as the sample stage or sample mount, as low as 10 K. A water recirculation cooling unit (Advanced Research System, Model CoolPac CP4), shown in Figure 17(b), was used to cool down the compressor. To control the temperature of the chamber, a resistive heater was used placed inside the cold head of the cryochamber. And the temperature was precisely set and maintained by a temperature controller (Lake Shore Cryotronics, Model 336) through a closed loop PID system. A control sensor (Lake Shore Cryotronics, Model DT-670B-SD) placed in close proximity of the heater was used as the feedback input for the PID loop.

Figure 16. *Advanced research system (ARS) Cryostat or cryogenic vacuum chamber.*

(a) (b) (c)

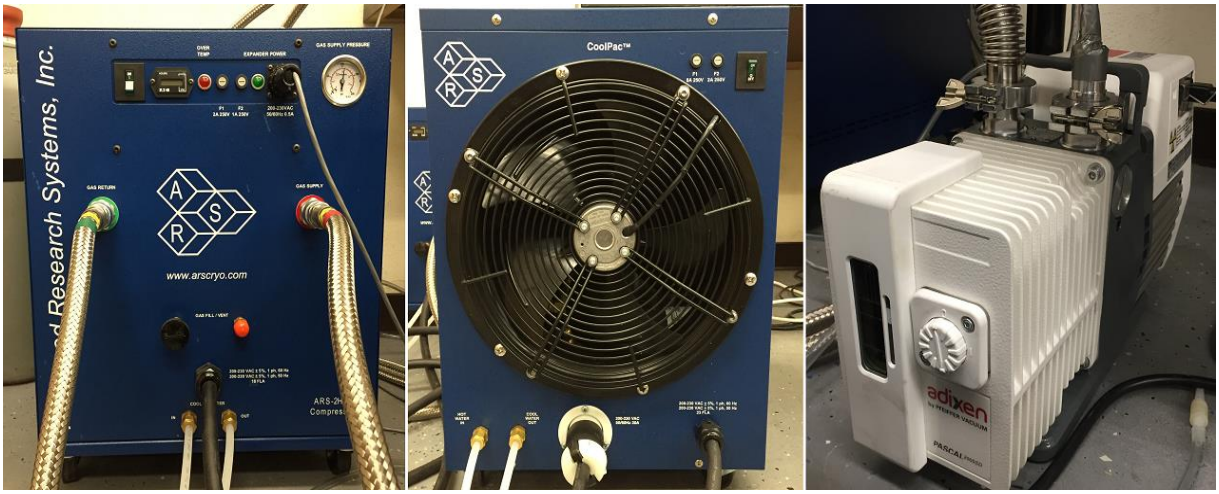

Figure 17. *Cryogenic vacuum chamber accessories: (a) compressor, (b) cooling unit, and (c) vacuum pump.*

3.2 Sample Holder

The schematic of the experimental setup and sample holder are shown in Figure 18. Typical size of the sample was 30 x 7 mm with a varying thickness. The base of the sample holder was made in layers from copper and a special machinable ceramic (Shapal Hi-M Soft, Precision Ceramics, Inc.) with high thermal conductivity (92 W/mK) for enhanced heat transfer, and high electrical resistivity (1 X 10^{15} Ω.cm @ 25°C) for electrical insulation. There are earlier reports of using cigarette paper [15] or Kapton foil [19] for the electrically insulating layer. However, the high thermal conductivity and mechanical strength of the ceramic (Shapal) helps for enhanced heat transfer and fast thermalization of the sample and holder. The copper base and two base supports made of copper accommodated 16 copper pins, which were electrically insulated by Teflon encasing. On top of the ceramic base, two copper blocks were placed that housed the cartridge heaters (Thorlabs, Model: HT15W). These heaters were used to heat the sample from either side. The copper blocks served as the heat source and sink while at the same time were used to make electrical contacts for electrical resistivity measurement. Four spring loaded cylindrical ceramic probe mounts were placed inside 4 holes in the copper blocks. The two voltage probes (thin Cu wire) and two RTD Cernox sensors (Lake Shore Cryotronics, Model: CX-1070-SD-HT-4M) were placed on top of these ceramic probe mounts and were mechanically pressed against the sample for voltage and temperature measurements, respectively.

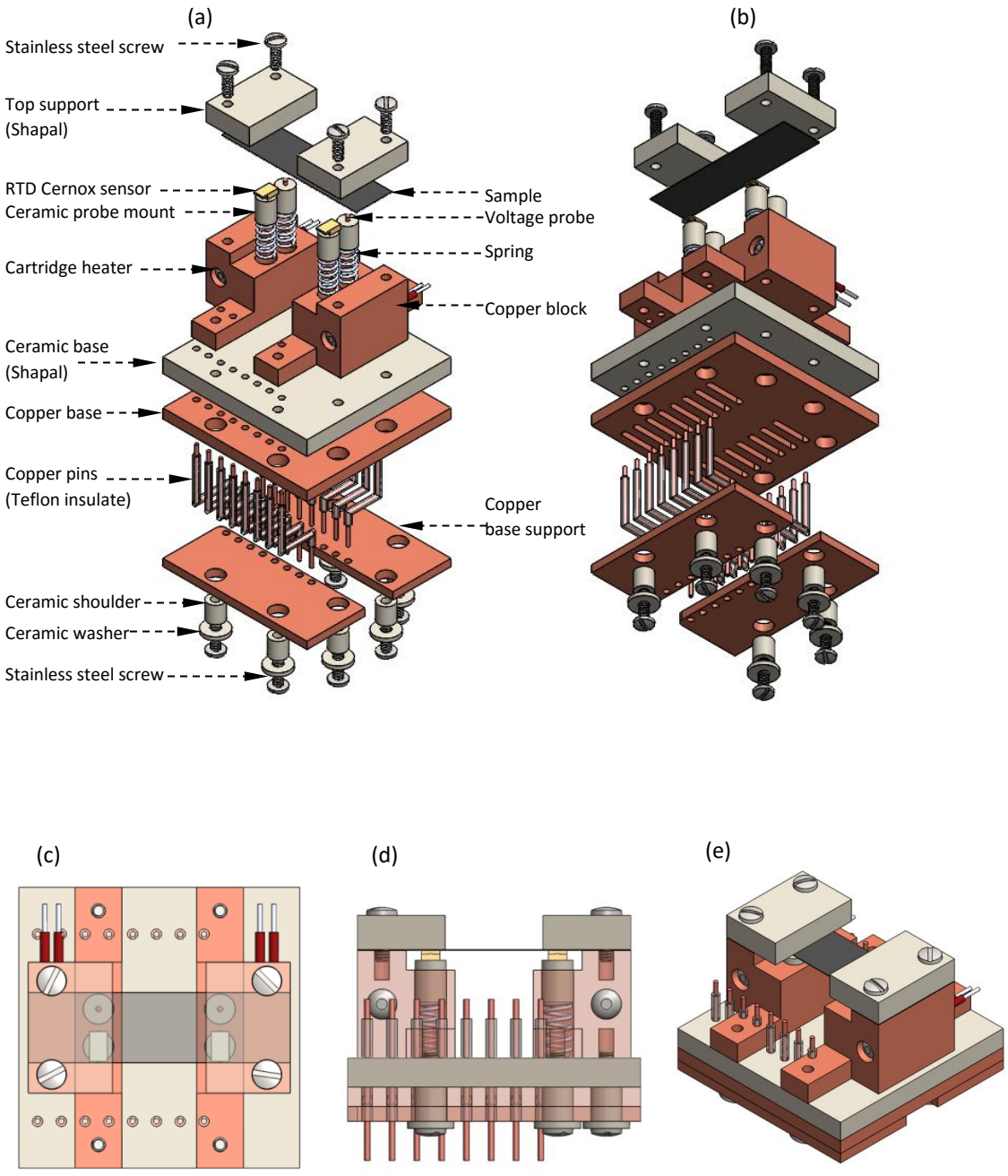

Figure 18. *SolidWorks design of the sample holder: (a) and (b) dismantled device showing different components and arrangements; (c) top view; (d) front view; (e) sample holder after assembly.*

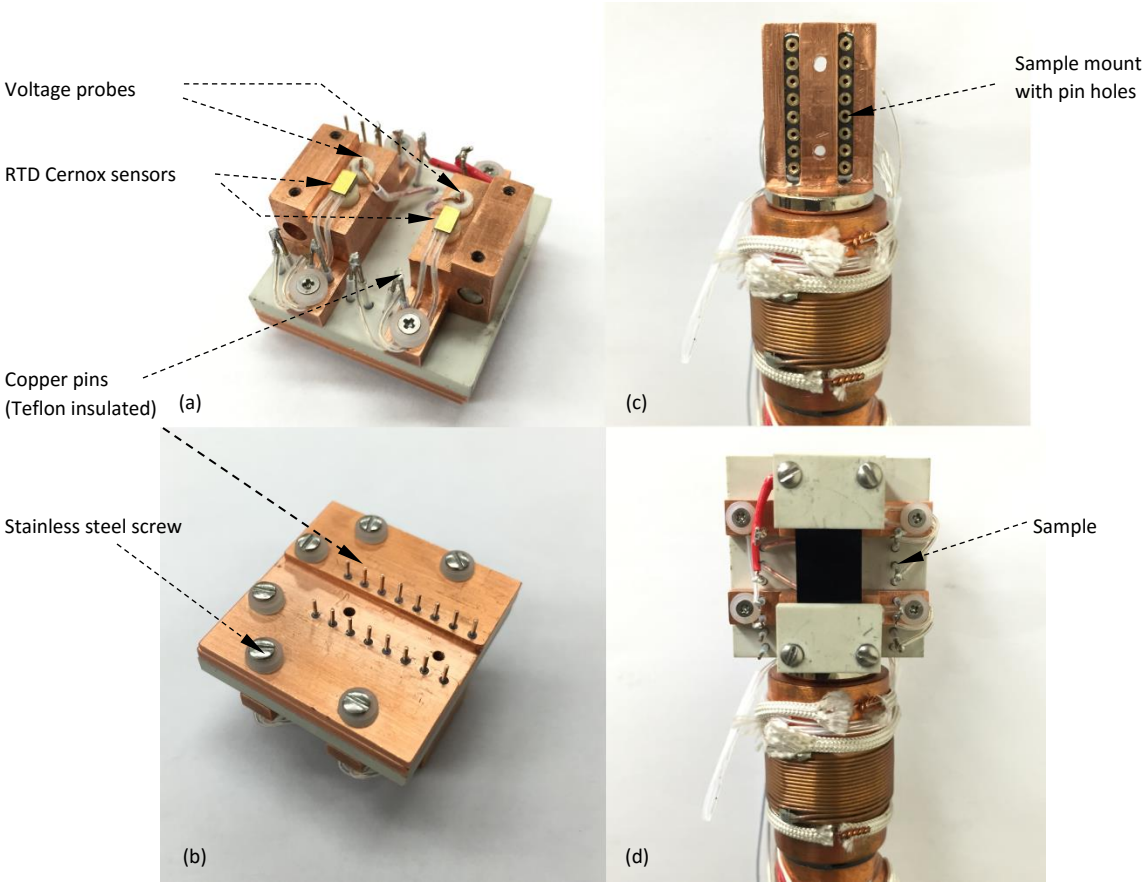

Figure 19. *Different views of the actual sample holder and sample mount: (a) sample holder without the top supports and a sample showing the measurement probes, (b) bottom side of the sample holder, showing the pins for plugging into the mount; (c) sample mount inside the cryostat; (d) sample holder plugged into the sample mount with a sample in place.*

Some earlier works [13,20,21] measured the temperature and voltage across the sample through embedded sensors inside the heat source and sink, avoiding direct contact with the sample. This approach introduces an error in the measurements by neglecting the inherent thermal and electrical contact resistance of the metal blocks and across the interface between metal block and sample [12]. The voltage probes were placed parallel and very close to the center of the RTD sensors to ensure the temperature of the voltage sensing points are identical to that of the RTDs. It was assumed that the temperature gradient in the sample was one-dimensional due to the special design of the device. However, due to the finite size of the RTDs, an assumption was made that the

temperature read by the RTDs are the temperature at the center of the contact surface. In addition, an elongated geometry was implemented in an effort to reduce dT/dz across the RTD-sample contact surface.[12] By using only Cu wire from sensing point to the external electronics, dissimilar metal junctions and hence the resulting Seebeck voltages in the circuit were avoided. Moreover, copper has a small change in its absolute thermopower between 10 and 400 K compared to Pt or Pb.[41,42] Using copper as the reference electrode, the reliability of the Seebeck measurements were increased. The rectangular sample was mounted on top of the polished copper blocks with the help of top support plates (ceramic), which were screwed to the copper blocks. This ensured good thermal and electrical contact between the copper blocks and the sample. This whole setup (sample holder) was plugged into the cold head, also called the sample mount, inside the cryostat (Figure 19). The temperature and voltage sensors were thermally anchored to the copper blocks to minimize heat flow through the sensors.

3.3 Temperature Measurement and Control

For accurate experimental results, the process of temperature measurement and control is very important. It is essential to know the absolute or average temperature of each measurement from 10 K to 400 K to see the changes in thermoelectric properties. It is also very important to accurately determine the temperature gradient along the length of the sample to ensure a zero thermal gradient for electrical resistivity measurements and a precisely measured gradient for thermopower or Seebeck coefficient measurements. First, vacuum was created inside the chamber and helium compressor was run to bring the chamber temperature to 10 K. As there was a radiation shield around the sample holder and the whole setup was under vacuum, the effect of thermal convection and

radiation was minimized, and assumed to be negligible. After the cryocooler was turned off, there was very good thermal stabilization and no gradient across the sample holder. The temperature of the sample and holder started to increase very slowly. The sample temperature was measured and controlled through a closed loop PID control by the temperature controller. The temperature control loop of the LabVIEW program measured the absolute temperature continuously and initiated the electrical resistivity and thermopower measurements at defined intervals. The temperature gradient during electrical resistivity measurements was measured to ensure a zero gradient across the length. For thermopower measurements, a temperature gradient was created using the cartridge heaters as control output and the two RTD sensors as control input. A maximum temperature difference (ΔT) of 1.0 K was created for the dV/dT or thermopower measurements which ensured no significant change in thermopower of the reference electrode (Cu). In the sample holder design, there was option to create the temperature gradient in either direction which helped to verify Seebeck results. The cartridge heater in the cold head of the chamber was used to continue measurements above room temperature. The heater was operated to raise and control the sample temperature at different setpoints up to 400 K while the measurements kept on running. Eventually the sample temperature was raised to 400 K and the measurements stopped.

3.4 Electrical Resistivity Measurement

The electrical resistivity of the sample was measured using standard dc four point method. Under this arrangement, small and constant current pulses (<0.1 A) with reversing polarity were sent through the cross section of the sample and the voltages were measured at two intermediate points along the length using the voltage probes. Just like

our room temperature measurements, this helped to avoid any resistive heating in thin samples and eliminated spurious Seebeck voltage that may cause erroneous electrical resistivity results. The two copper blocks (heat source and heat sink) acted as the current contacts at two ends along the sample length. This is a special combined mode (delta mode) operation of the Keithley 6220 Current Source and Keithley 2182A Nanovoltmeter. The electrical resistivity is then calculated using equation (2). The advantage of sending small current pulses is that it does not heat up thin samples. Also continuously reversing the polarity of the current pulses helps get rid of spurious Seebeck voltages that may cause erroneous electrical resistivity results. Several voltage readings were averaged when calculating the electrical resistivity.

3.5 Seebeck Coefficient Measurement

For Seebeck coefficient measurement, one-dimensional in-plane temperature gradient was created along the length of the sample by heating it from one side, and the temperature difference at two points (12 mm apart, along the length) was measured with the RTD sensors. Two voltage probes placed parallel and in close proximity (<1 mm) to the temperature sensors measured the voltage difference across them. The negative ratio between the induced voltage and the temperature difference is defined as the Seebeck coefficient or thermopower. The measured voltage difference across the input terminals of the nanovoltmeter can then be expressed as:

$$\Delta V = -\left(\int_{T_0}^{T_c} S_{ref}\, dT + \int_{T_C}^{T_H} S\, dT + \int_{T_H}^{T_0} S_{ref}\, dT\right) \tag{5}$$

Where S is the Seebeck coefficient of the sample, S_{ref} is the Seebeck coefficient of the reference voltage probes, which in this case are copper, T_0 is the ambient or room

temperature, T_H and T_C are the hot and cold side temperatures of the sample where the voltage probes make contact with the sample. A detail explanation on the above equation can be found in references.[17, 31] Now for the reference probes, we have

$$\int_{T_0}^{T_c} S_{ref}\, dT + \int_{T_H}^{T_0} S_{ref}\, dT = \int_{T_H}^{T_c} S_{ref}\, dT \tag{6}$$

which simplifies equation (3) to be

$$\Delta V = -\left(\int_{T_C}^{T_H} S\, dT + \int_{T_H}^{T_c} S_{ref}\, dT\right) = -\int_{T_C}^{T_H} \left(S - S_{ref}\right) dT \tag{7}$$

For small temperature differences ($\Delta T < 1$), we can assume the Seebeck coefficient value of the sample and reference probes to be constant. Assuming $T_{av} = \frac{T_H + T_C}{2}$ and $\Delta T << T_{av}$, equation (7) further simplifies to

$$S(T_{av}) = -\frac{\Delta V}{\Delta T} + S_{ref}(T_{av}) \tag{8}$$

In our case, the reference probes were copper. So, S_{ref} is actually S_{Cu}. Based on the above equation, the absolute Seebeck coefficient of the sample was calculated where S_{Cu} is given by the expression[17]

$$S_{Cu}(T) = 0.041T\left[exp\left(-\frac{T}{93}\right) + 0.123 - \frac{0.442}{1 + \left(\frac{T}{172.4}\right)^3}\right] + 0.804 \tag{9}$$

Here the thermopower is expressed in μVK^{-1} and the temperature in Kelvin. The uncertainty of the thermoelectric scale of copper in the above equation is $\pm 0.1\ \mu VK^{-1}$ in the temperature range of 70 K – 900 K[17]. A graphical representation of the interpolation function is presented in Figure 20 with comparison to previously reported literature data. We can see that the data are comparable to as low as 70 K. However, below 70 K the

interpolation function is not reported to be accurate. Moreover there are reports about the low temperature anomaly in the Seebeck coefficient of copper below 50 K, which is evident from the data of Gold et al.[42] and MacDoanld et al.[43] This can produce some differences at low temperature thermopower measurements when using copper as the reference material. A detail discussion on the low temperature anomaly in thermopower of copper can be found in the reference.[42]

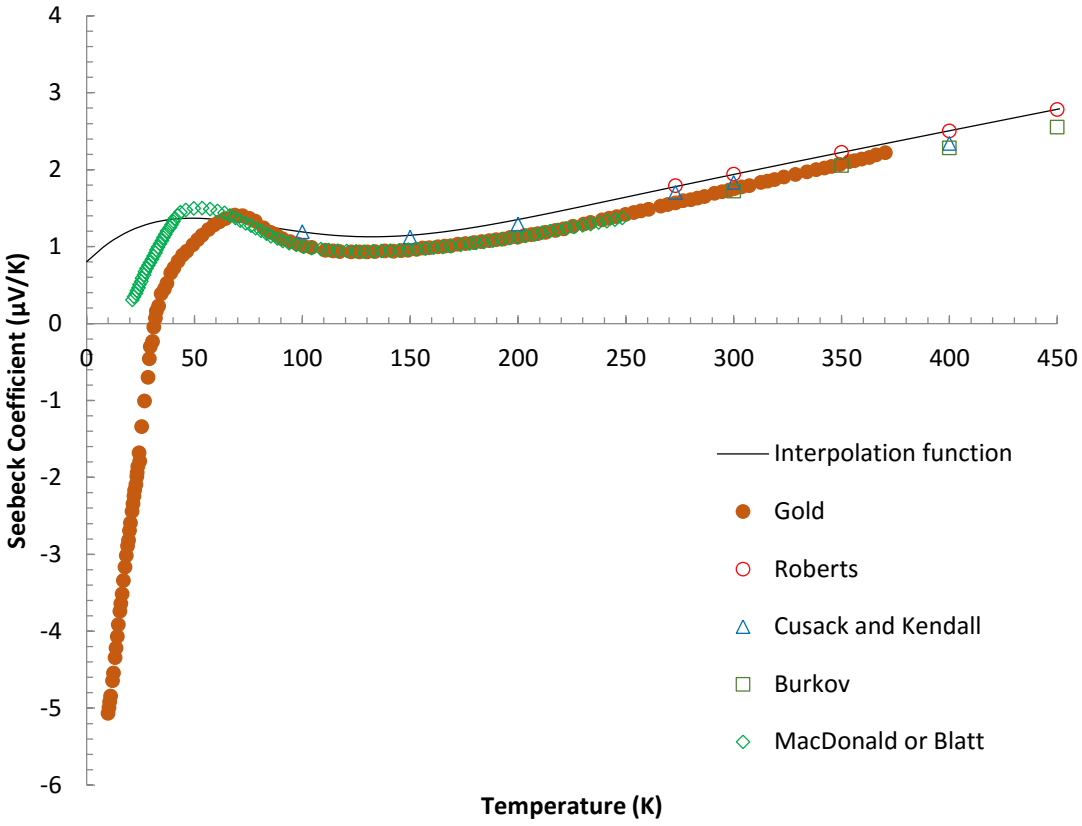

Figure 20. *Thermopower or Seebeck coefficient of pure copper as a function of temperature. Solid line represents the interpolation function; hollow circles represent data from Roberts [44]; squares from Burkov et al. [17]; triangles from Cusack and Kendall [41]; diamonds from MacDonald [43] and Blatt [45]; and filled circles from Gold et al. [42]*

3.6 Measurement and Data Acquisition with LabVIEW

Keithley 6220 Current Source, Keithley 2182A Nanovoltmeter and LakeShore 336 Temperature Controller were used for the current, voltage and temperature measurements, respectively (Figure 21). The setup was interfaced with a computer for full automation of the experiments. Commercial software LabVIEW was used to control the experiments and to do the data acquisition and calculation.

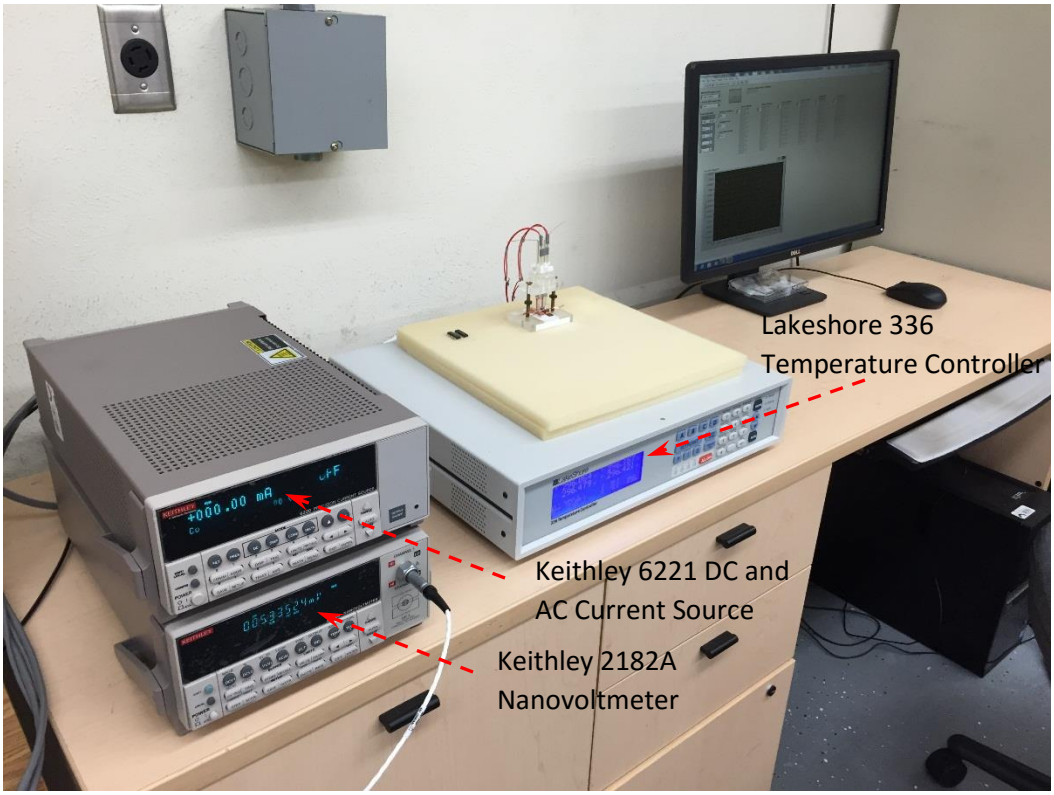

Figure 21. *Measurement and data acquisition devices: DC Precision Current Source, Nanovoltmeter, Temperature Controller and Computer with the LabVIEW program.*

A LabVIEW program was developed to control the experiment and automate the execution. All the control parameters can be set from the main front panel or graphical user interface (Figure 38) of the program and the experiment can be run or stopped from here. Also the user can see the real time measurement data from the front panel. The

program reads and processes data from the data acquisition devices, displays them on the front panel and writes them to files for future use. The block diagram is the backbone of the program where all the graphical programming is done. The main VI consists of several subVIs to make the program easy to understand and to keep the main block diagram neat and concise. The main VI calls upon these subVIs in order of their sequence of execution set in the main VI. In Figure 37, the flow chart describes the order of execution of the tasks by the LabVIEW program. Figures 38, 39, 40, 41, 42, 43 and 44 show the front panel and block diagram of the main VI, and block diagrams of the subVIs for resistivity measurement, thermopower measurement, all RTD reading, single RTD reading and heater configuration, respectively.

3.7 Validation and Results

In order to calibrate the apparatus and validate the results, some reference material with known Seebeck and electrical resistivity values in 10-400 K range had to be used. In our case, pure nickel (Ni) film was used for this purpose. Nickel has been often used for validating such apparatus and has a distinct trend of Seebeck coefficient and electrical resistivity values from 10 K to 400 K. The measurement results are reported in Figure 22 and 23 for electrical resistivity and Seebeck coefficient respectively. As we can see from Figure 22, the experimental results for electrical resistivity of nickel are in excellent agreement with the values reported by Laubitz et al[36], White et al[46], and Burkov et al.[17]

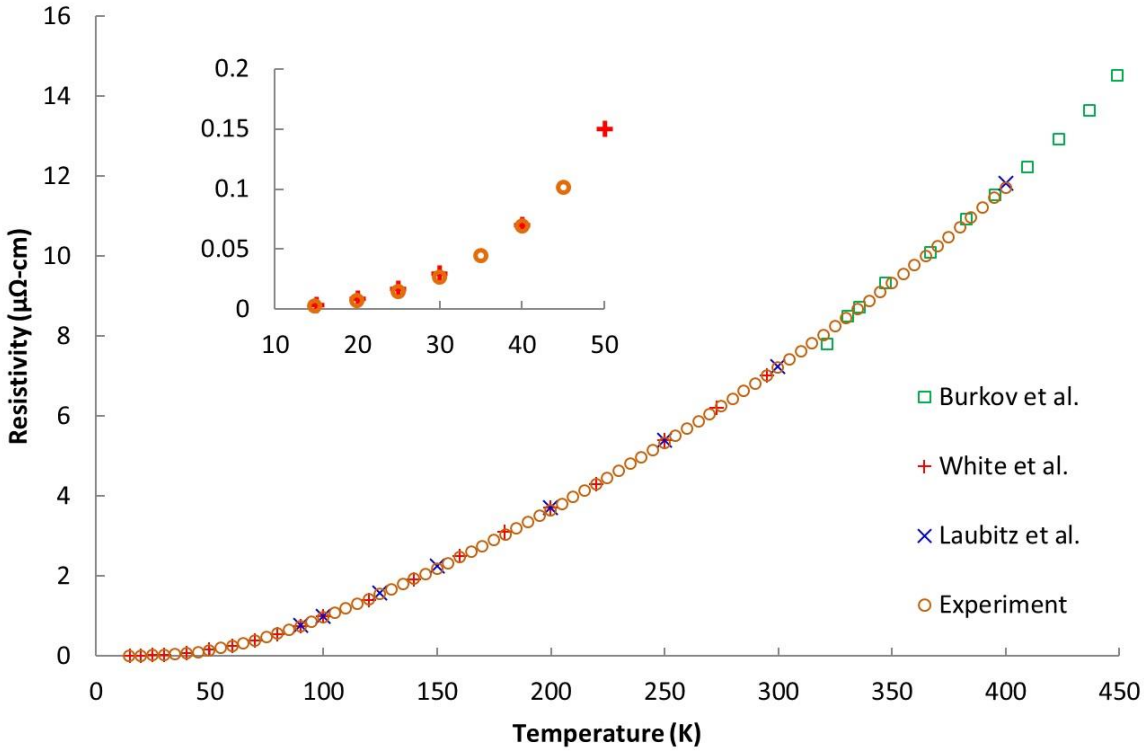

Figure 22. *Electrical resistivity of nickel measured using the cryogenic device and compared to previously reported data. Squares represent the data from Burkov et al. [17], pluses from White and Woods [46], crosses from Laubitz et al. [36], and circles represent the experimental data. Inset is the magnified plot over the 10-50 K range.*

In the case of thermopower, our experimental results for pure nickel are presented in Figure 23, comparing to a number of literature data to cover our temperature range of interest and to accommodate an acceptable range of values at different temperatures. The slight deviation among the reported values is quite expected because thermopower is a highly sensitive parameter to measure that varies with temperature, measurement principle, accuracy and sensitivity of the measurement apparatus, reference probe and associated reference thermopower used. However, it is very obvious from the graph that the reported values follow a certain trend and fall between narrow ranges. Considering

these circumstances, it can be said that our experimental results are in close agreement with the literature values.

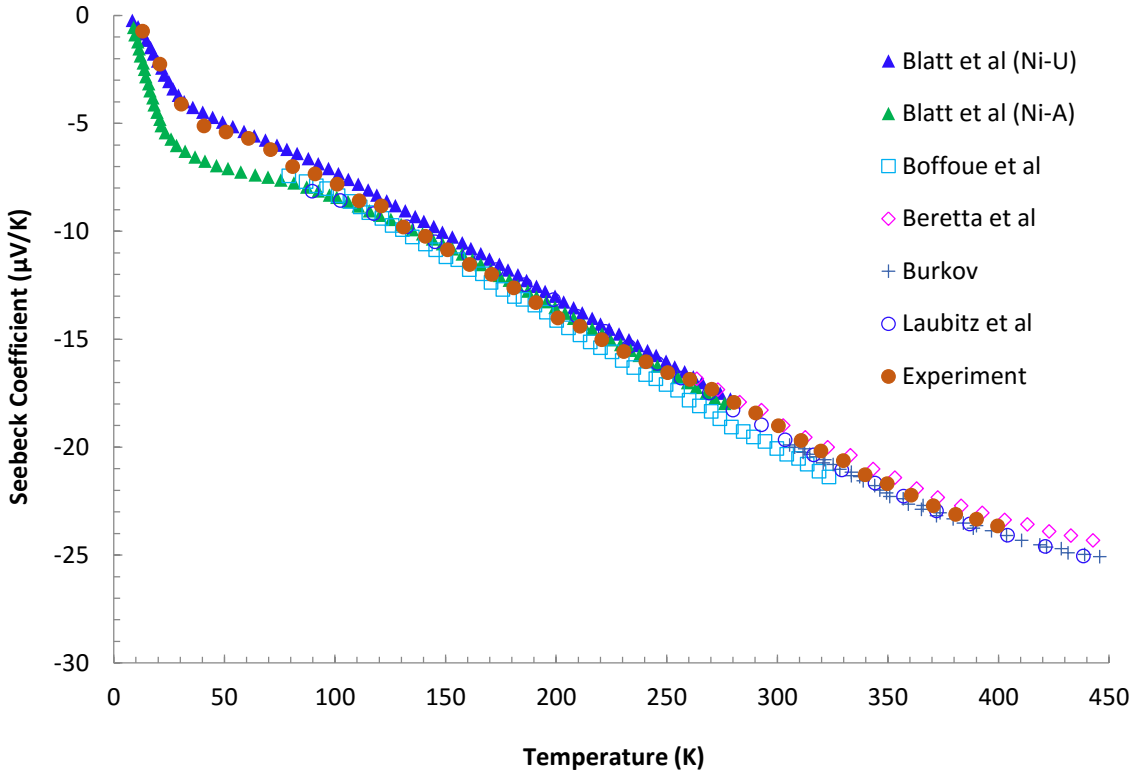

Figure 23. *Absolute Seeebck coefficient of nickel compared to previously reported data. Blue and green triangles are from Blatt et al.* [47] *for unannealed and annealed Ni, respectively; squares from Boffoue et al.* [15]*; diamonds from Beretta et al.* [19]*; pluses from Burkov et al.* [17]*; hollow circles from Laubitz et al.* [36]*; and filled circles are the results of this study.*

CHAPTER 4: FINITE ELEMENT MODELING

4.1 FEM Model

After choosing a set of suitable materials for the sample holder, a SOLIDWORKS model of the sample holder with specific design details was developed. However, an important issue to address was the interfaces between the different materials of dissimilar thermal and mechanical properties. These materials included copper, a special machinable ceramic (commercial name: Shapal), ceramic washer and shoulder (alumina) and stainless steel screws. Inevitably, there were differences in thermal and structural responses and as a result, thermal stresses were supposed to develop. In order to assess the thermal and structural response of the sample holder and to evaluate its structural integrity over the working temperature range, a finite element model of the sample holder was developed using the ANSYS finite element methods (FEM) commercial package. The CAD model was simplified for ANSYS simulations by removing the pins and simplifying some intricate design parts in order to save some computation time. The meshed FEM model is shown in Figure 24. From the design point of view, the main concerns were the temperature distribution and thermal stabilization rate of the holder and sample, as well as the induced thermal stresses in copper and ceramic parts.

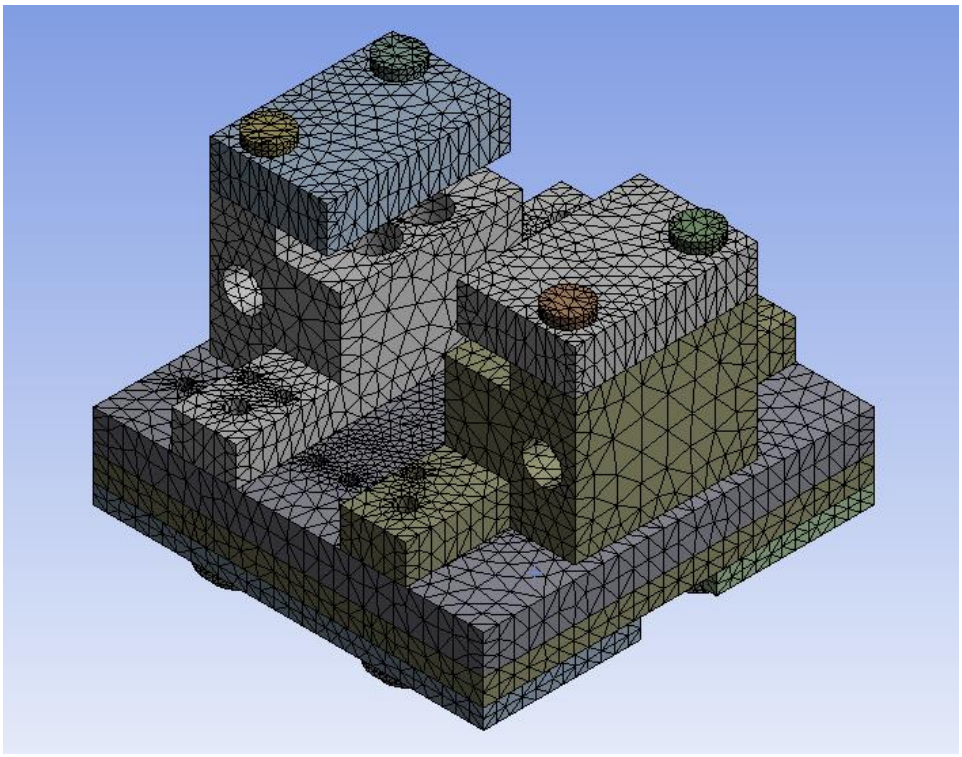

Figure 24. *Finite element model of the sample holder after meshing.*

A set of boundary conditions resembling those of experiments was used for the simulations. Thermal radiation was assumed to be zero as a radiation shield was used in actual experiment. The sample holder was also placed in vacuum inside the chamber and convection effects were negligible. Convection heat transfer was therefore assumed to be zero in the model. A perfectly insulated boundary condition was applied to the whole sample holder. Heat flux was applied to the bottom of the sample holder through the embedded heater in the sample mount. Figure 25 shows how heat is transferred to and from the sample holder in the direction of the red and blue arrows, respectively. During heating, heat is supplied to the sample holder in the direction of red arrows. Conversely, while cooling, heat transfer takes place in the opposite direction (blue arrows). The top ceramic supports, ceramic base, and the copper base are modeled to be in compressive loading by the screws. Each screw is assumed to exert 412 N force. Instead of defining

the input heat flux, the temperature at the bottom of the sample mount at various time intervals was experimentally determined through a RTD sensor. This data was then used as an input for the simulation to determine the thermal and structural response of the sample holder.

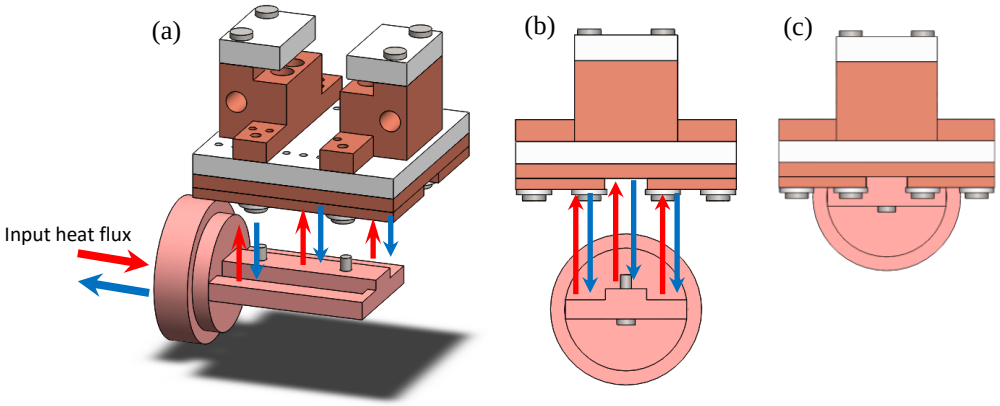

Figure 25. *Direction of input heat flux: (a) sample holder and sample mount dismantled, showing the direction of heat flux; (b) dismantled view from the right hand side; (c) sample mount and holder connected together.*

4.2 Temperature Distribution

The thermal response (temperature distribution), cooling and heating rate of the sample holder, and the resulting thermal stresses were calculated at different temperatures. Copper has a very high thermal conductivity (especially at low temperatures) that should facilitate faster thermal stabilization of the sample holder. Shapal is a special engineered ceramic made from aluminum nitride and boron nitride that has excellent thermal and mechanical properties and can be machined easily to make intricate design parts. The ceramic's high thermal conductivity and electrical insulation was very desirable for the design.

The temperature distribution and von misses stress distribution across the sample holder, cooled down to 10 K in 50 minutes, are shown in Figures 26 and 27.

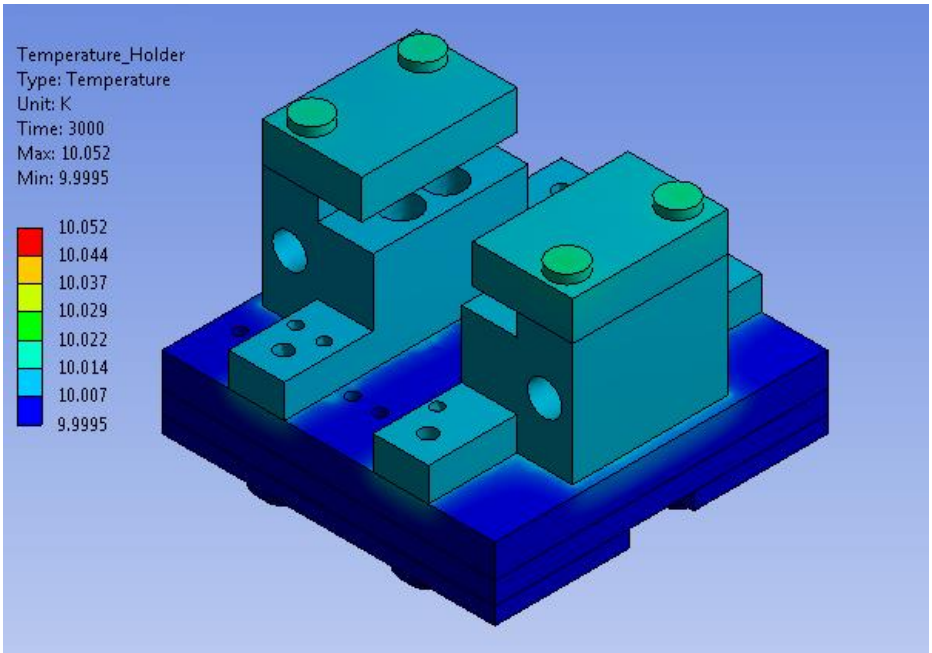

Figure 26. *Temperature distribution across the sample holder when cooled down from room temperature to 10 K in 50 mins.*

From the temperature distribution model in Figure 26, it is observable that the temperature is quite evenly distributed and stabilized across the sample holder considering that this is a transient analysis. The considerably high thermal conductivity of the special Shapal ceramic and the very high thermal conductivity of copper at low temperature played important role in the fast thermal stabilization of the structure. The maximum temperature region is located in the alumina washer parts at the bottom which is negligible. However, this is a very ideal case considering 100% thermal contact and no interface resistances in the contact regions between parts. In practice, there will not be 100% contact and thermal interface resistances will be present. But after doing the practical demonstration, the actual thermal response and stabilization time was found to be very fast and close to the computational model.

4.3 Thermal Stresses

The calculated thermal stresses in the copper parts at 10 K are shown in Figure 27. The equivalent von Mises stresses were calculated and compared with the yield stresses of copper at different temperatures. The maximum equivalent von Mises stress for the copper (oxygen free copper) parts was found to be 121.4 MPa, which is considerably lower than its yield stregth of 400 MPa at 4 K reported by Copper Development Association Inc. For Shapal, the strength of the material at low temperatures is not reported in the literature. However, the sample holder was able to withstand the thermal load without any structural failure during the validation process. Stress analysis at 400 K was also carried out and the results were also acceptable. From the thermal and structural simulations, the design of the sample holder was found to be reliable for operation from 10K to 400 K.

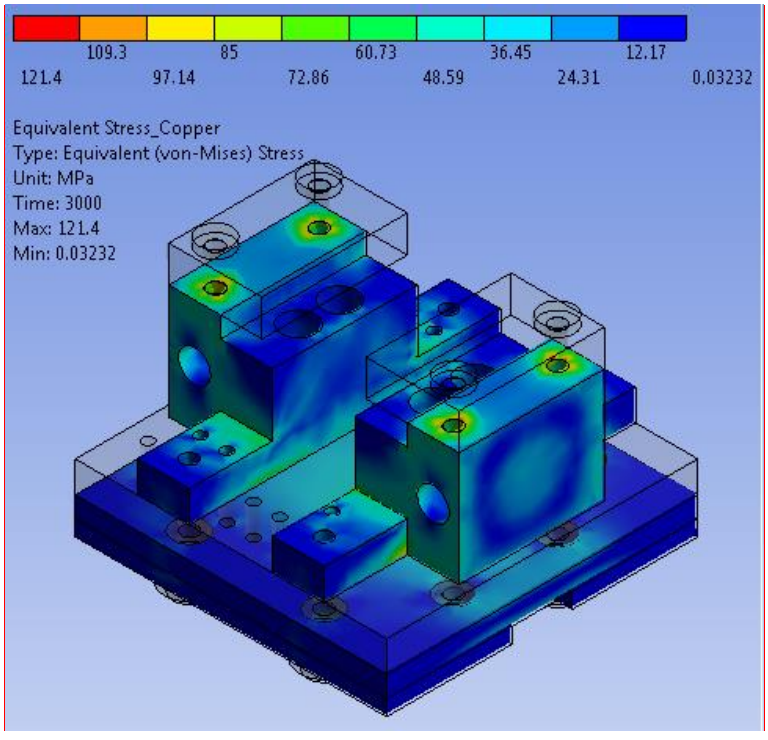

Figure 27. *Equivalent von-Mises stress across the copper parts of the sample holder.*

4.4 Convergence Study

Mesh conversion studies were performed on the model, the results for which are plotted in Figure 28. For analytical purposes, the equivalent stresses across the Shapal parts and the steel screws with increasing number of mesh elements were examined. The results converged for more than 30,000 elements and therefore a mesh with 35,000 elements was used for all the simulations.

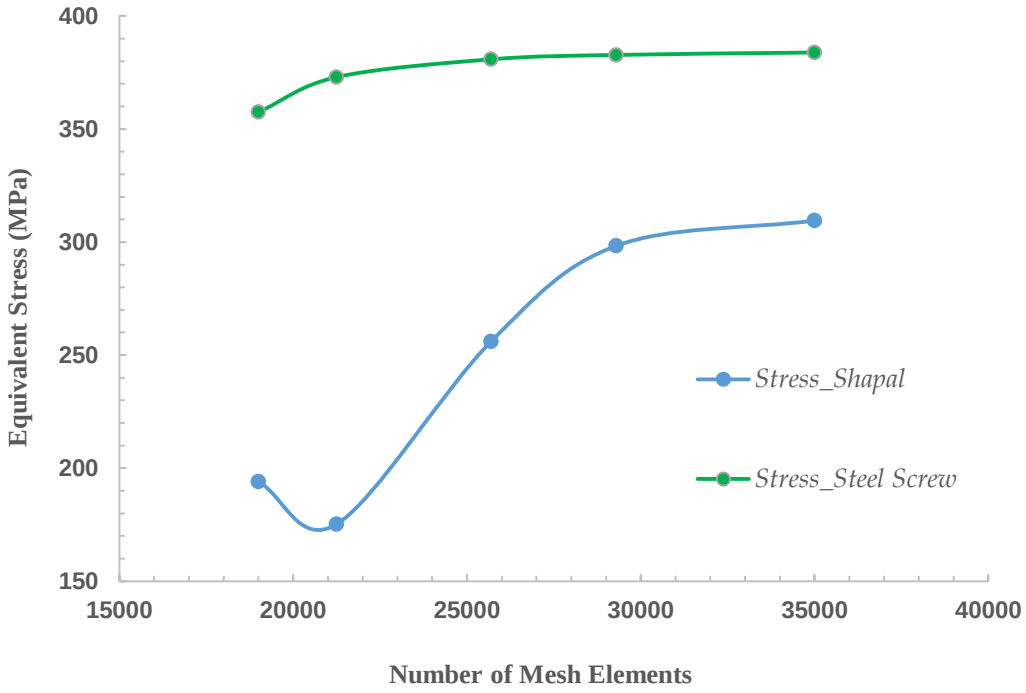

Figure 28. *Mesh convergence study of the FEM simulation*

CHAPTER 5: ORGANIC SAMPLE CHARACTERIZATION

5.1 Conducting Polymer for Organic Thermoelectrics

PEDOT:PSS is one of the most promising electrically conducting polymers with applications in many low-cost high volume devices, including flexible electrodes, electro-chromic displays, transistors and organic thermoelectrics.[48-51] Among the important properties of this polymer are its intrinsic high electrical conductivity, the ability to tune the conductivity, transparency to light in thin films, mechanical flexibility, electrochemical, thermal, and oxidative stability.[52] Currently, PEDOT:PSS holds the highest thermoelectric efficiency among pure polymer thermoelectrics.[51] One promising method to improve the electrical conductivity of PEDOT:PSS has been identified as doping with organic solvents, such as dimethyl sulfoxide (DMSO), ethylene glycol (EG), poly(ethylene glycol) (PEG), or sorbitol, in an aqueous dispersion of PEDOT:PSS.[51, 53-59] Moreover, conductivity of PEDOT:PSS films can be further improved by immersion in polar solvents or exposure to their vapors.[51, 55] Unfortunately, there is not a clear understanding of how the presence of the dopants in the polymer solution or solvent treatment of dried films alters the morphology and functionality of the PEDOT:PSS film. This understanding is, however, critical to developing processing protocols that cannot only improve, but optimize the performance of PEDOT:PSS. It is clear that a crucial first step is to correlate the morphology of the PEDOT:PSS to its performance.

Several conceptual models to explain doping of PEDOT:PSS with polar organic solvents have been presented.[53, 55, 58-62] Among these, a change in the conformation of the PEDOT chain, removal of excess insulating PSS, and a decrease in the Coulombic

interaction between PEDOT and PSS chains upon doping have received the most attention. Most structural studies, to date, employ surface characterization techniques such as atomic force microscopy (AFM) and X-ray photoelectron spectroscopy (XPS) or bulk methods that do not have the resolving power to distinguish between PEDOT and PSS phases[53, 55, 63, 64] to elucidate the bulk morphology of PEDOT:PSS. For example, Ouyang et al. attributed the enhanced conductivity of PEDOT:PSS films with doping of organic solvents, such as ethylene glycol, 2-nitroethanol, methyl sulfoxide or 1-methyl-2-pyrrolidinone, to the enhanced inter chain interaction among the PEDOT chains.[53] This increased interaction is purported to be the result of changes in the PEDOT conformation from a coil to an extended coil or linear structure.[53] AFM and XPS studies by Jonsson et al. [60] attribute the enhanced performance of PEDOT:PSS films doped with sorbitol, isopropanol or NMP to the removal of excess PSS that resides in an insulating "PSS-shell" surrounding the conducting PEDOT:PSS grains. The loss of this PSS leads to a better connectivity between the conducting grains in the film. Kim et al. noted that the incorporation of polar organic solvents such as DMSO, DMF or THF enhanced the charge carrier properties of PEDOT:PSS free standing membranes.[59] They credit the enhanced characteristics to a solvent-induced screening effect that reduces the Coulomb interaction between positively charged PEDOT chains and negatively charged PSS chains.[59] Similarly, Ashizawa et al.[58] investigated the charge carrier characteristics of PEDOT:PSS as a function of the amount of polar solvent that is added to the PEDOT:PSS mixture. The enhanced charge carrier properties in these studies were attributed to the reduced effective energy barrier for hopping of charge carriers between localized PEDOT states.[58] It is interesting that the solvent treatments not only enhance

the functional performance but also alter the mechanical properties. Okuzaki et al. showed that EG treatment of PEDOT:PSS microfibers enhanced both electrical and mechanical properties, which were attributed to molecular changes in the PEDOT domains from an amorphous state to a crystalline state.[62] Very recently, Ouyanget et al.[65] studied the conformational changes in a drop-casted PEDOT:PSS film at microscale and concluded that PSS forms a transparent rim around PEDOT:PSS film. These investigations, however, do not discuss the changes in the bulk morphology of PEDOT:PSS that occur in presence of a polar solvent. A more thorough understanding of the changes to the PEDOT:PSS with pre- and post-solvent processing is needed to optimize the performance of PEDOT:PSS in many applications. This understanding can be indirectly achieved by studying the temperature dependent behavior of thermoelectric properties in organic samples.

5.2 Sample Preparation

PEDOT:PSS in form of 1.3 % dispersion in water (Clevios PH1000) was used for sample preparation. PEDOT to PSS ratio was reported to be 1 to 2.5. Some of the doping mimicked those reported in the recent work by Kim et al.[4], which reported the highest recorded thermoelectric figure-of-merit for poly(3,4-ethylenedioxythiophene): poly(styrenesulfonate) (PEDOT:PSS). Different solvent pre- and post-treatments were done to investigate the effects on the electrical conductivity and Seebeck coefficient of these organic samples, at room temperature and in the 10-400K range. The following samples with different pre- and post-treatments were prepared: (1) Pristine PEDOT:PSS; (2) PEDOT:PSS post treated with EG; (3) PEDOT:PSS mixed with 5vol% EG in the pre-deposition solution; (4) PEDOT:PSS mixed with 5vol% EG in the pre-deposition solution

and post treated with EG; (5) PEDOT:PSS post treated with H_2SO_4; and (6) PEDOT:PSS mixed with 5vol% EG in the pre-deposition solution and post treated with H_2SO_4 . In this procedure, the PEDOT:PSS aqueous solution was first doped with 5 vol% of EG in the pre-deposition solution. The resulting solution was sprayed on Polyethylene Terephthalate (PET) substrate (DuPont Teijing Films) to form a thin film. For the spray coating, the PET substrate was continuously rotated while spraying to ensure uniform thickness. After spray coating, the sample was annealed at 120 °C for 15 minutes inside a vacuum oven. After annealing, it was immediately put into an EG bath at 60 °C for 2 hours. The process was followed by annealing for an extra15 minutes at 120 °C. For the H_2SO_4 post treatment, the thin film samples were heated up to 160 °C, and treated with small amount of H_2SO_4 drops for 5 minutes. The samples were then washed with Deionized water (DI water) and dried for 5 minutes on a hot plate at 160 °C. In addition to the aforementioned samples, a carbon nanotube-polymer composite sample was prepared. For this, 20 mg of double-walled carbon nanotube (DWCNT) was mixed with 65 mg of PEDOT:PSS and sonicated at 40 kJ. The process was followed by centrifuging for 1 hour at 3000 rpm. The resulting solution was spray coated on a PET substrate and dried at room temperature. For Seebeck coefficient and electrical resistivity measurements in the 10-400 K range, gold was sputtered on the sample in the form of four stripes to ensure good thermal and electrical contact with the probes. A typical PEDOT:PSS sample prepared for cryogenic measurement is shown in Figure 29.

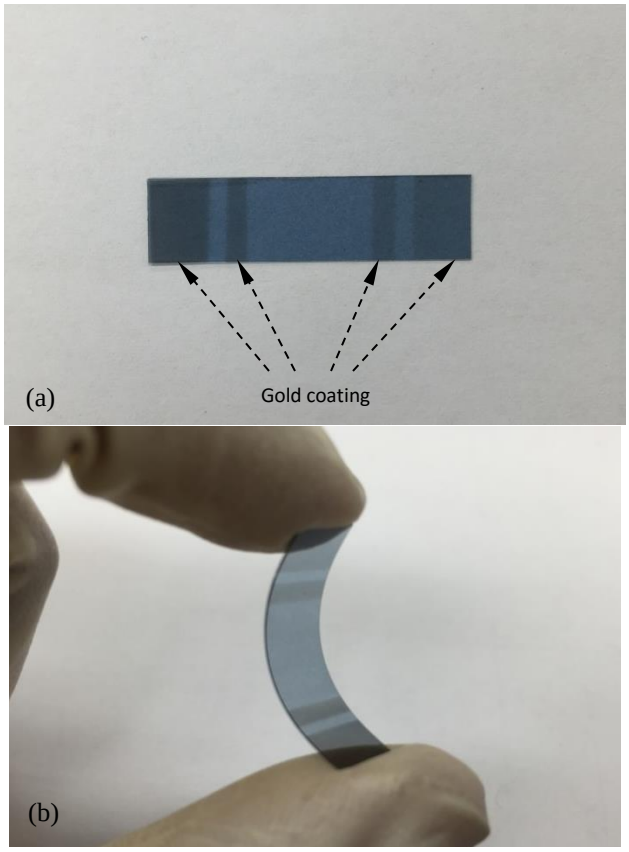

Figure 29. *Representative organic thin film sample for characterization in 10-400 K: (a) showing the gold coating for thermal and electrical contact; (b) flexible thin film on PET substrate.*

For the room temperature measurements, two pieces from the same sample were prepared for electrical conductivity and Seebeck coefficient measurements. For electrical conductivity measurement, four thin strips of silver paint were deposited on samples to ensure Ohmic contact with the voltage and current probes (Figure 30(a)). For Seebeck measurement, four silver paste dots (Figure 30(b)) were placed on the sample to ensure good contact with the thermocouples and the voltage probes.

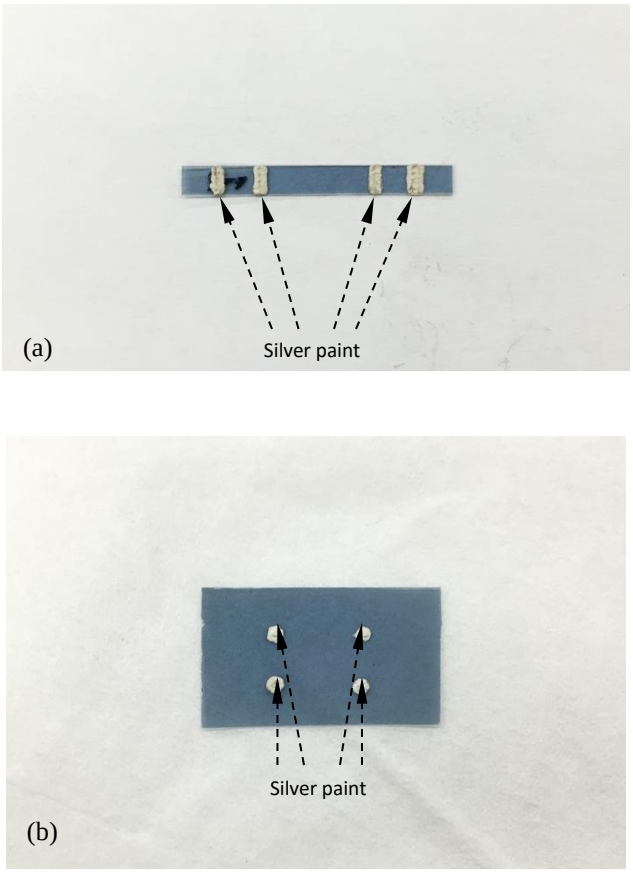

Figure 30. *Organic thin film samples for characterization at room temperature: (a) sample for electrical conductivity measurement showing the silver strips for electrical contact; (b) sample for Seebeck coefficient measurement showing silver dots for good thermal and electrical contact.*

5.3 Seebeck Coefficient and Electrical Resistivity Results

Both the room temperature and cryogenic apparatuses were used for different measurements. Room temperature characterization allows for fast screening of samples and to decide whether to perform the much longer measurements over 10-400 K range. All samples were characterized at room temperature, and only the PEDOT:PSS mixed with 5vol% EG, and the CNT mixed PEDOT:PSS samples were characterized in the 10-400K temperature range. The experimental results for the room temperature Seebeck coefficient and electrical conductivity measurements are provided in Figures 31 and 32, respectively. In comparison to the Seebeck coefficient of the pristine PEDOT:PSS

samples, there were not much improvement observed when the samples were pre-treated with EG. However, EG post-treatment increased the Seebeck coefficient of the samples. In terms of H_2SO_4 post-treatment, the Seebeck coefficient of the samples decreased slightly. From Figure 32, great improvement in electrical conductivity was observed with all pre- and post-treatments compared to pristine PEDOT:PSS. Highest electrical conductivity of 1082 S/cm was found for sample (4), PEDOT:PSS mixed with 5vol% EG in the pre-deposition solution and post treated with EG.

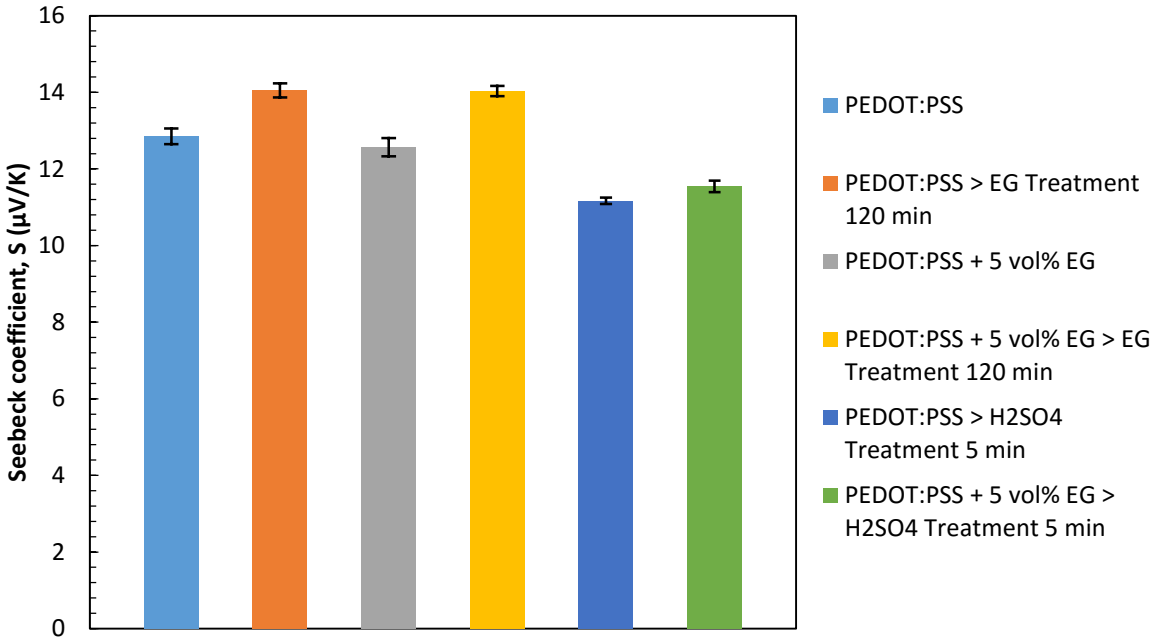

Figure 31. *Seebeck coefficient of different organic samples at room temperature.*

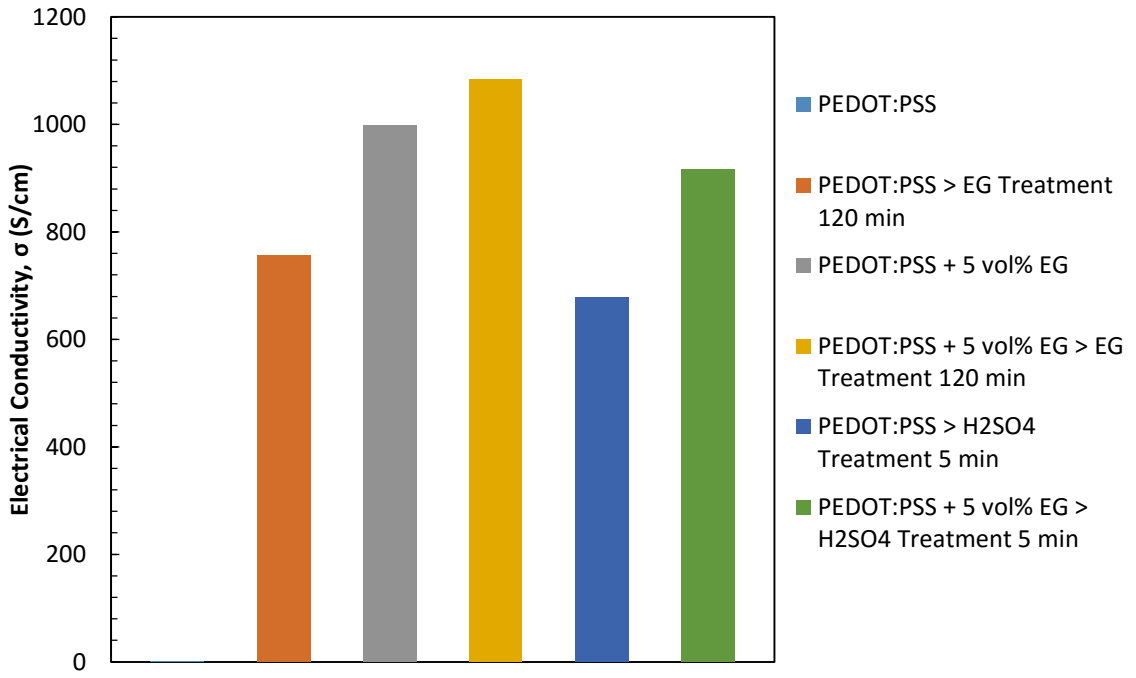

Figure 32. *Electrical conductivity of different organic samples at room temperature.*

The experimental results for the measurements in the 10-400 K range are provided in Figure 33-36. Electrical resistivity and Seebeck coefficient of a PEDOT:PSS sample mixed with 5vol% EG are provided in Figure 33 and 34. From the results, one could see the distinct trend in electrical resistivity and Seebeck coefficient as the temperature was varied from 10 K to 400 K.

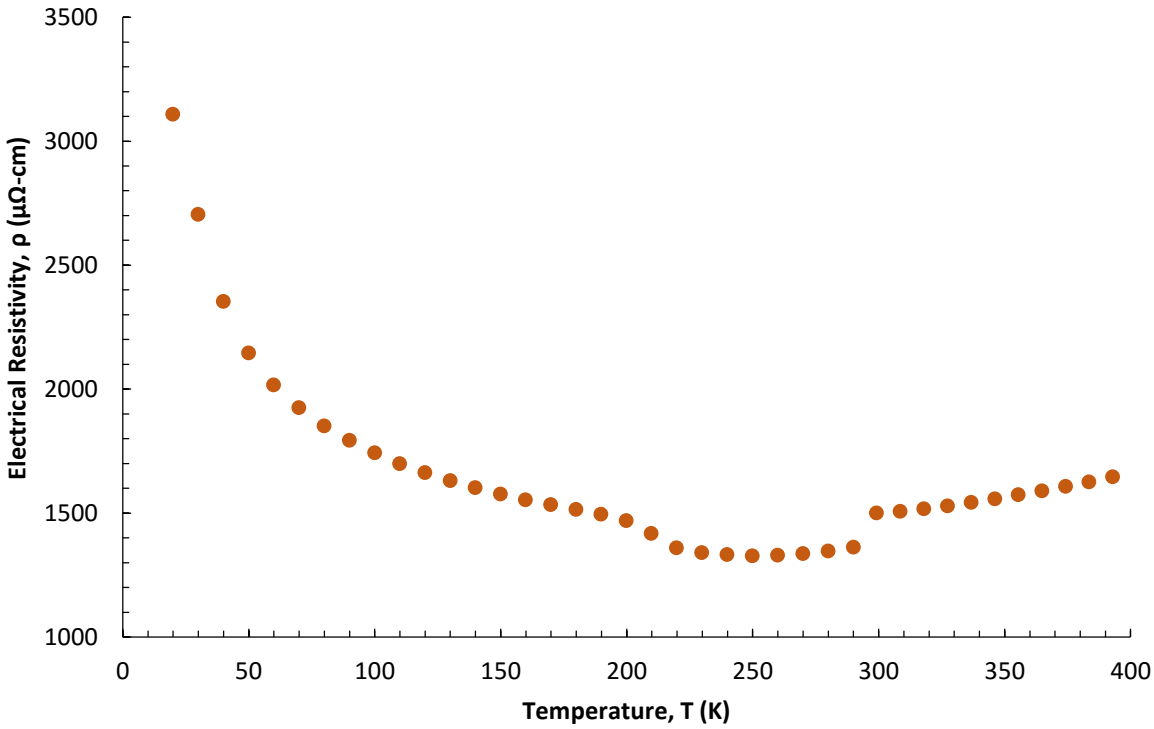

Figure 33. *Electrical resistivity of the 5vol% EG mixed PEDOT:PSS sample in the 10-400 K temperature range.*

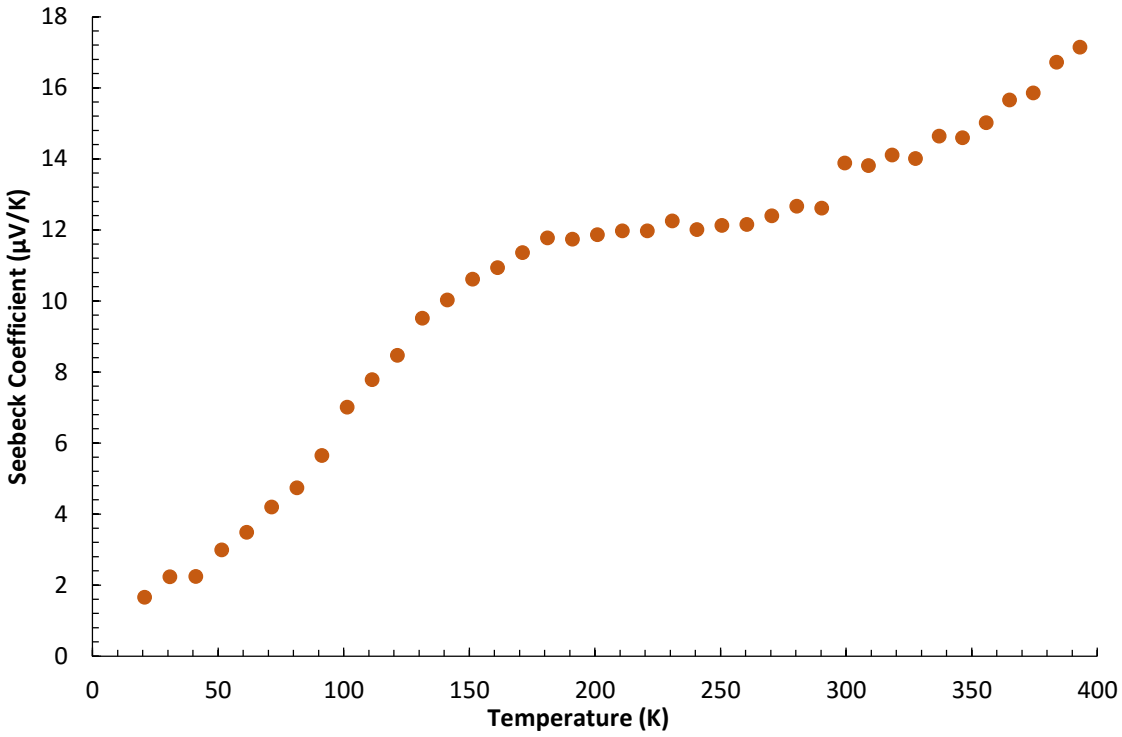

Figure 34. *Seebeck coefficient of the 5vol% EG mixed PEDOT:PSS sample in the 10-400 K temperature range.*

We have also investigated the effect of the inclusion of highly conductive CNT fillers into the PEDOT:PSS matrix. The measured electrical resistivity and Seebeck coefficient of a PEDOT:PSS sample mixed with double-walled carbon nanotubes (DWCNT) are provided in Figure 35 and 36. From the results, it is evident that the inclusion of CNTs considerably increased the Seebeck coefficient of PEDOT:PSS. Again a distinct trend in electrical resistivity and Seebeck coefficient is observed as the temperature was varied from 10 K to 400 K.

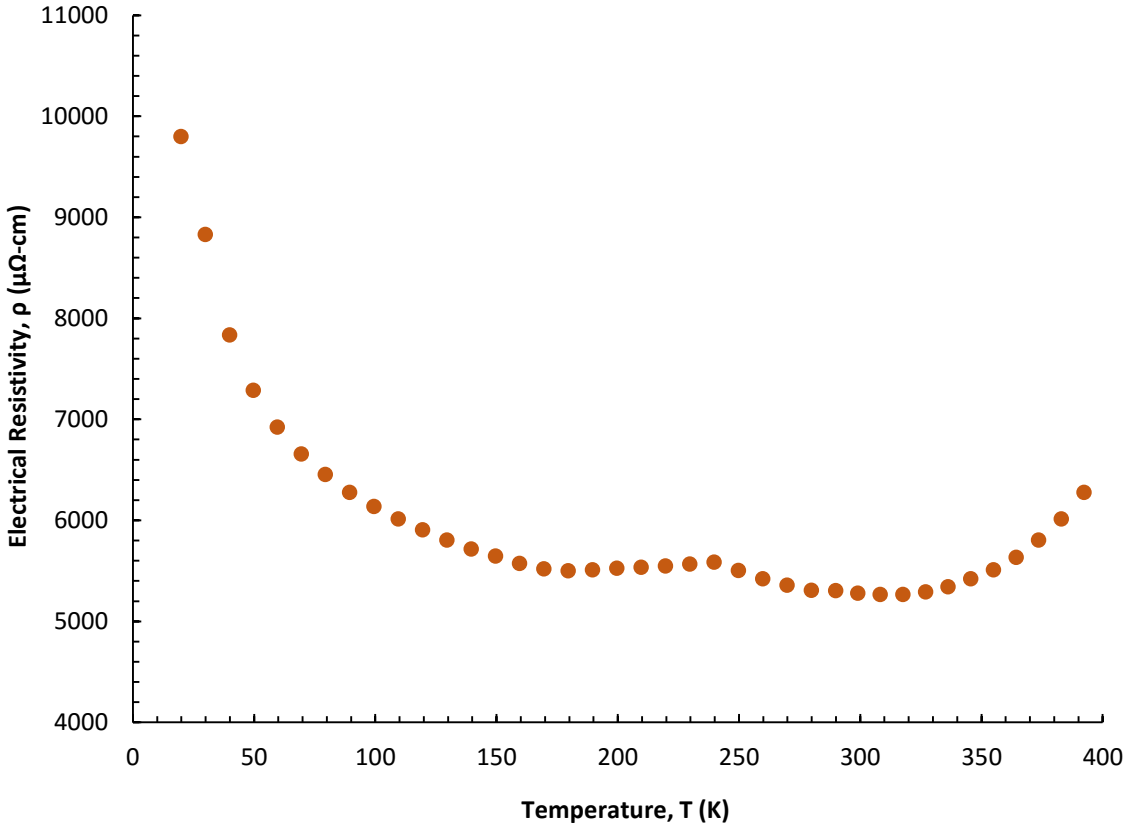

Figure 35. *Electrical resistivity of the DWCNT-PEDOT:PSS sample in the 10-400 K temperature range.*

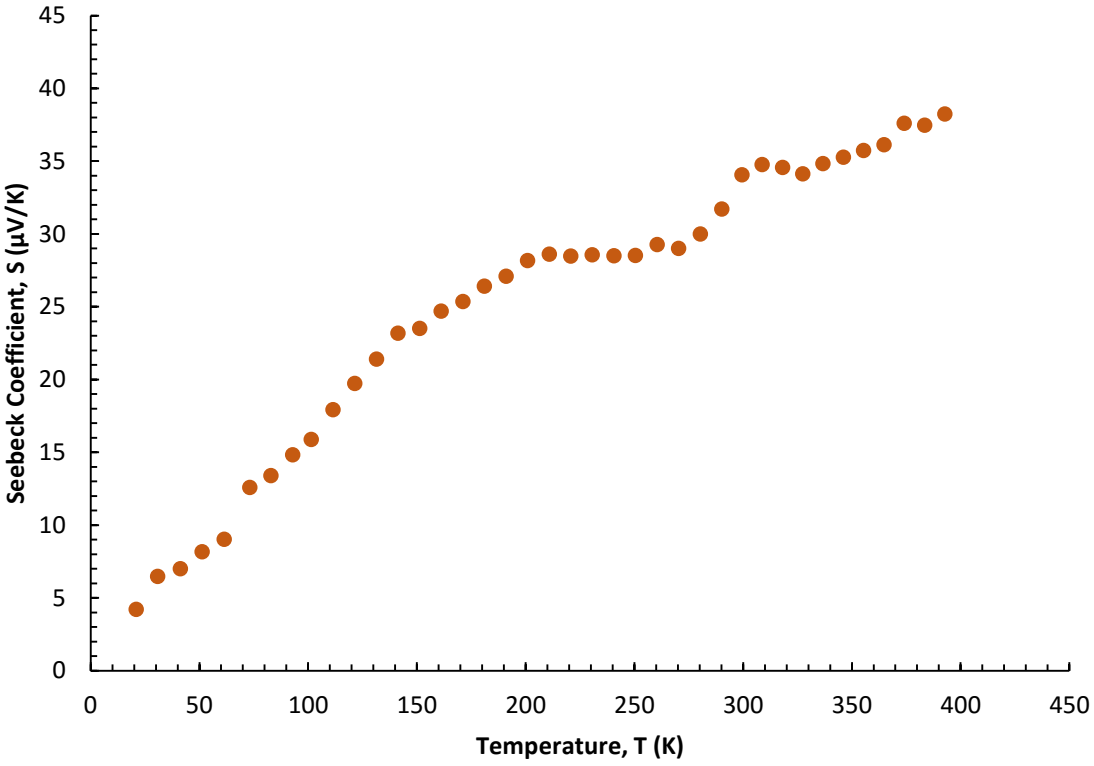

Figure 36. *Seebeck coefficient of the DWCNT-PEDOT:PSS sample in the 10-400 K temperature range.*

CHAPTER 6: CONCLUSION AND FUTURE WORK

An experimental apparatus for the simultaneous measurement of thermopower and electrical resistivity over the 10–400 K was designed and developed. The apparatus is suitable for the thermoelectric characterization of both organic and inorganic materials, in the shape of thin film or bulk samples. Using the spring mounted pressure contact for the sensors, the reusability of the sensors and setup was demonstrated. In contrast with the previous efforts, this also helps reuse a sample to check for repeatability of measurements over a wide range of temperatures. This is a key feature that proves the reliability of the apparatus. In addition, incorporation of RTD sensors instead of thermocouples increases the accuracy of the measurements. The RTDs are also advantageous for pressure mounting soft materials such as organic samples considering their flat surface, unlike the thermocouples. To validate our apparatus, we have measured the thermopower and electrical resistivity of pure nickel, and compared our experimental results with previously reported values. The measured values are in excellent agreement to the previously reported values in literature. The greatest source of error in the thermopower measurement may come from any improper thermal contact between the RTD and the sample. Using pressure contacts, we have mostly eliminated that error. The other source can be the spurious thermoelectric voltage in the electrical circuit and the finite contact size of the RTDs. However, the differential dV/dT method of thermopower measurement implemented here gets rid of any voltage offset present in the circuit. For electrical resistivity measurements, errors mostly arise from the dimensional measurements such as the thickness of the sample and the distance between voltage probes. Through very careful and precise measurements, these errors can be eliminated from considerations.

Further improvements of organic materials will be impeded until a comprehensive knowledge of their processing-structure-thermoelectric property relationships is developed. Future work will include characterization of various organic thermoelectrics using this unique characterization capability at UNM.

APPENDIX

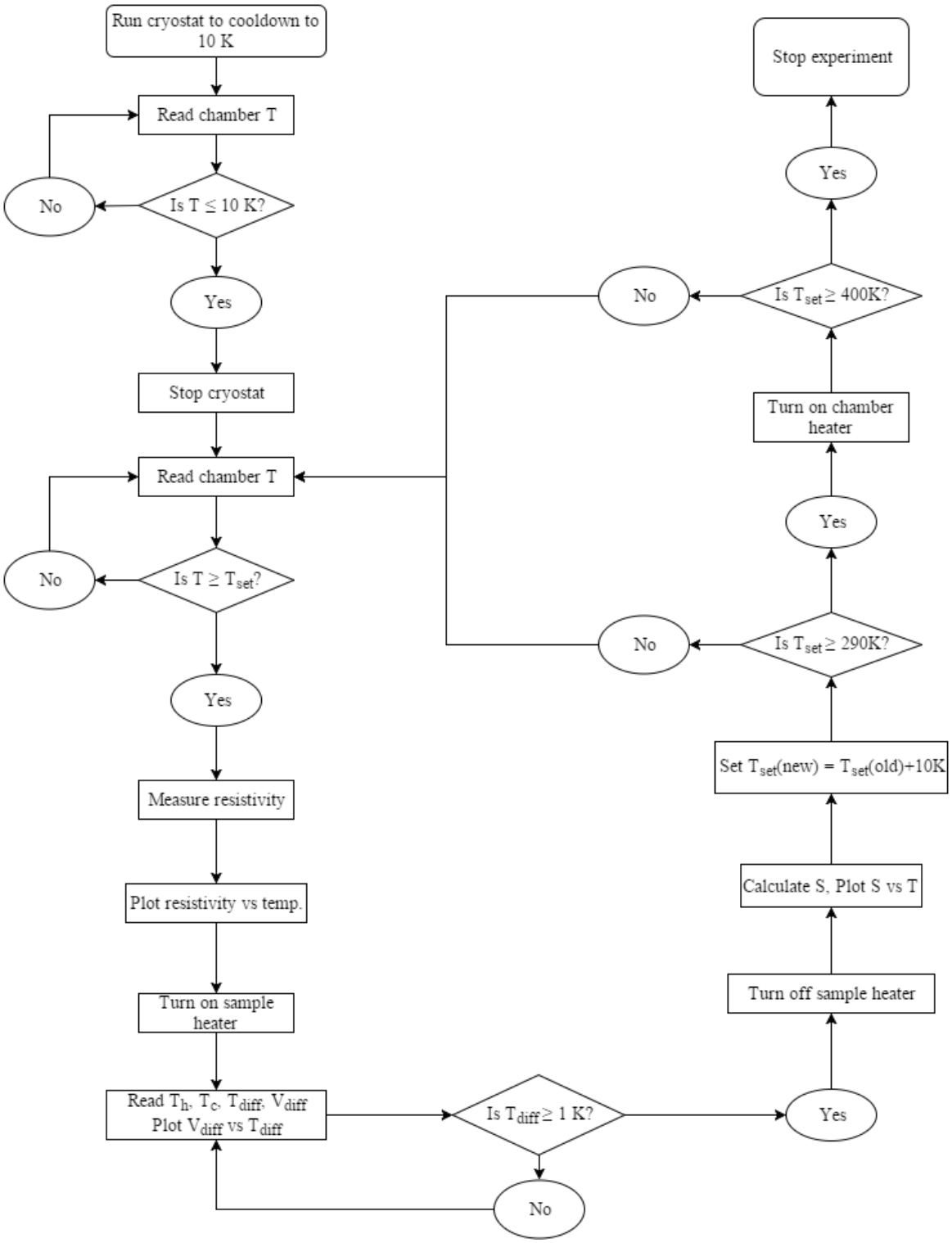

Figure 37. *Block diagram (flow chart) of the experimental control and data acquisition process.*

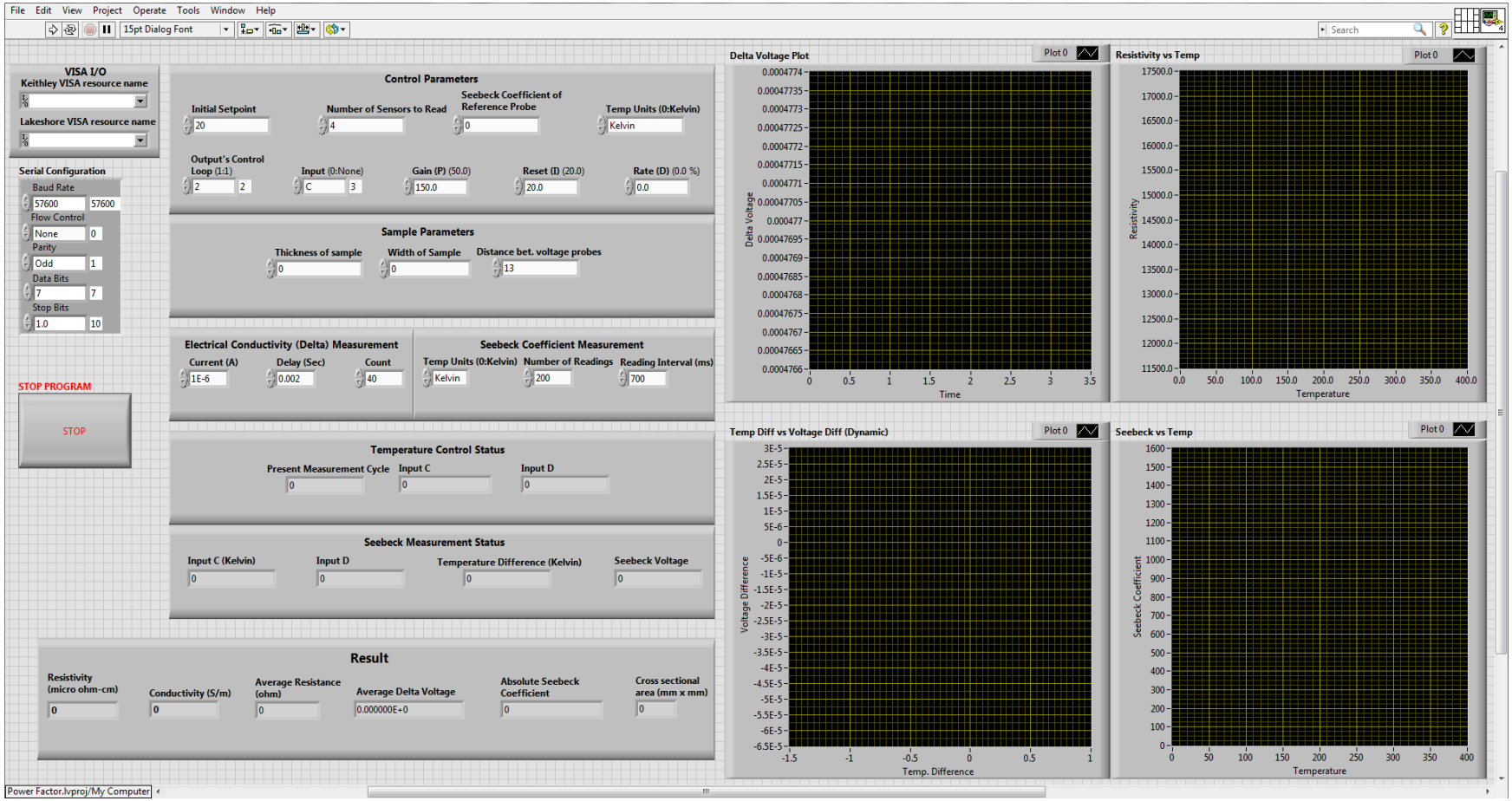

Figure 38. *Front panel of the main VI of the LabVIEW program.*

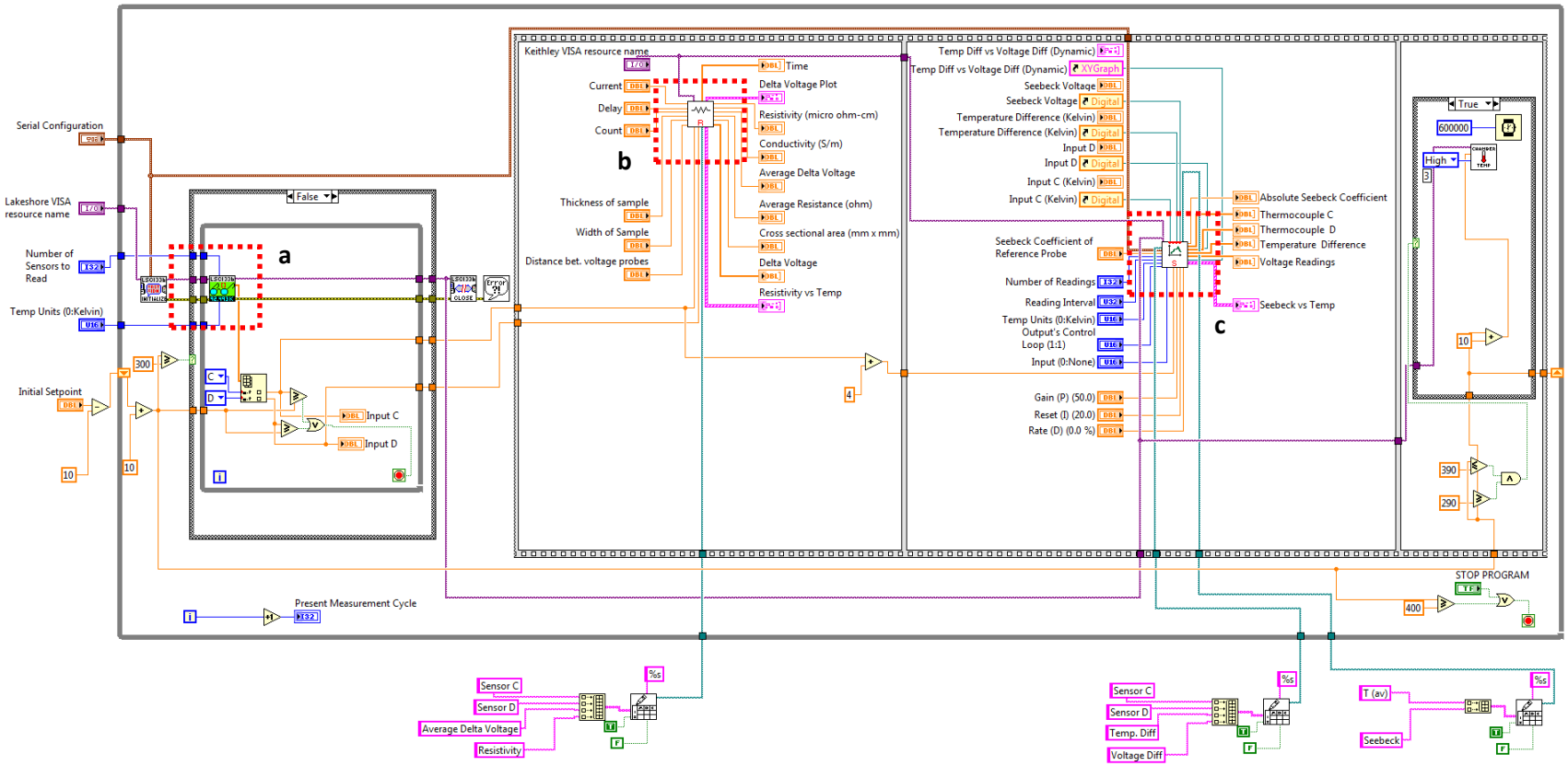

Figure 39. *Block diagram of the main VI of the LabVIEW program. The red boxes shows the SubVIs:(a) SubVI to read temperature data from 4 RTD sensors; (b) SubVI for electrical resistivity measurement; (c) SubVI for Seebeck coefficient measurement.*

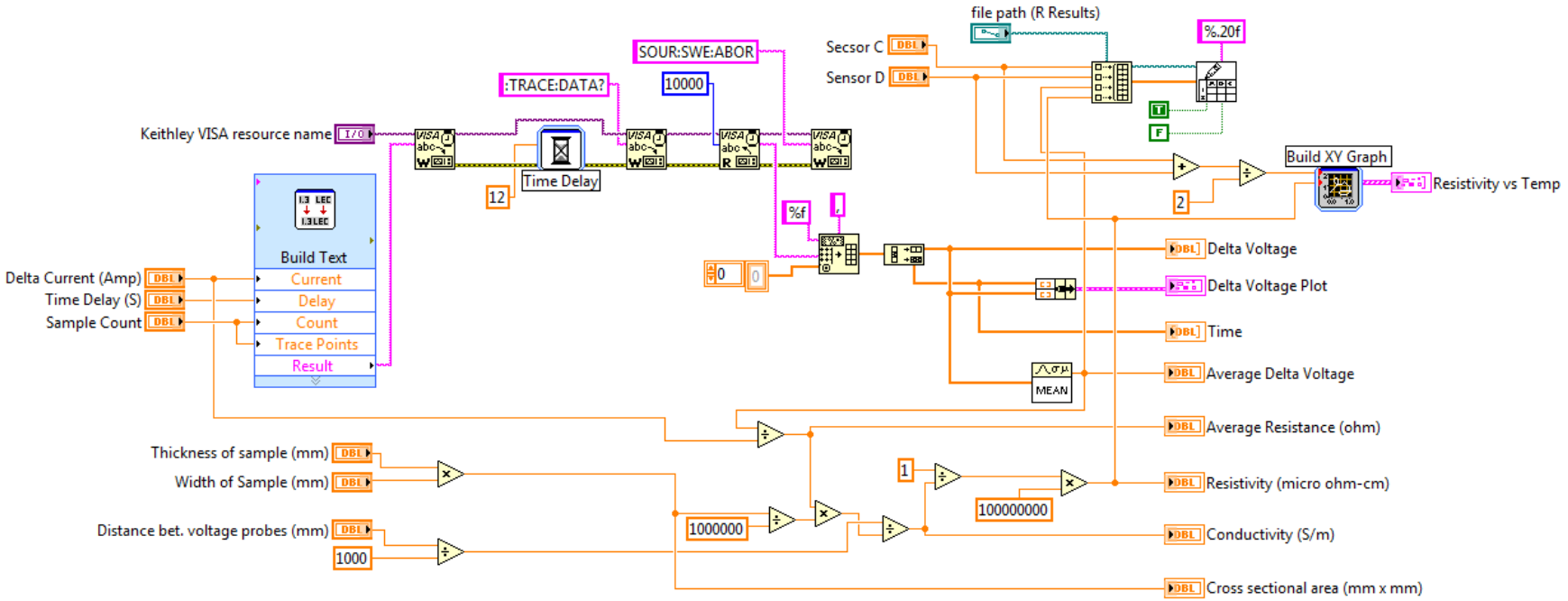

Figure 40. *SubVI for electrical resistivity measurement.*

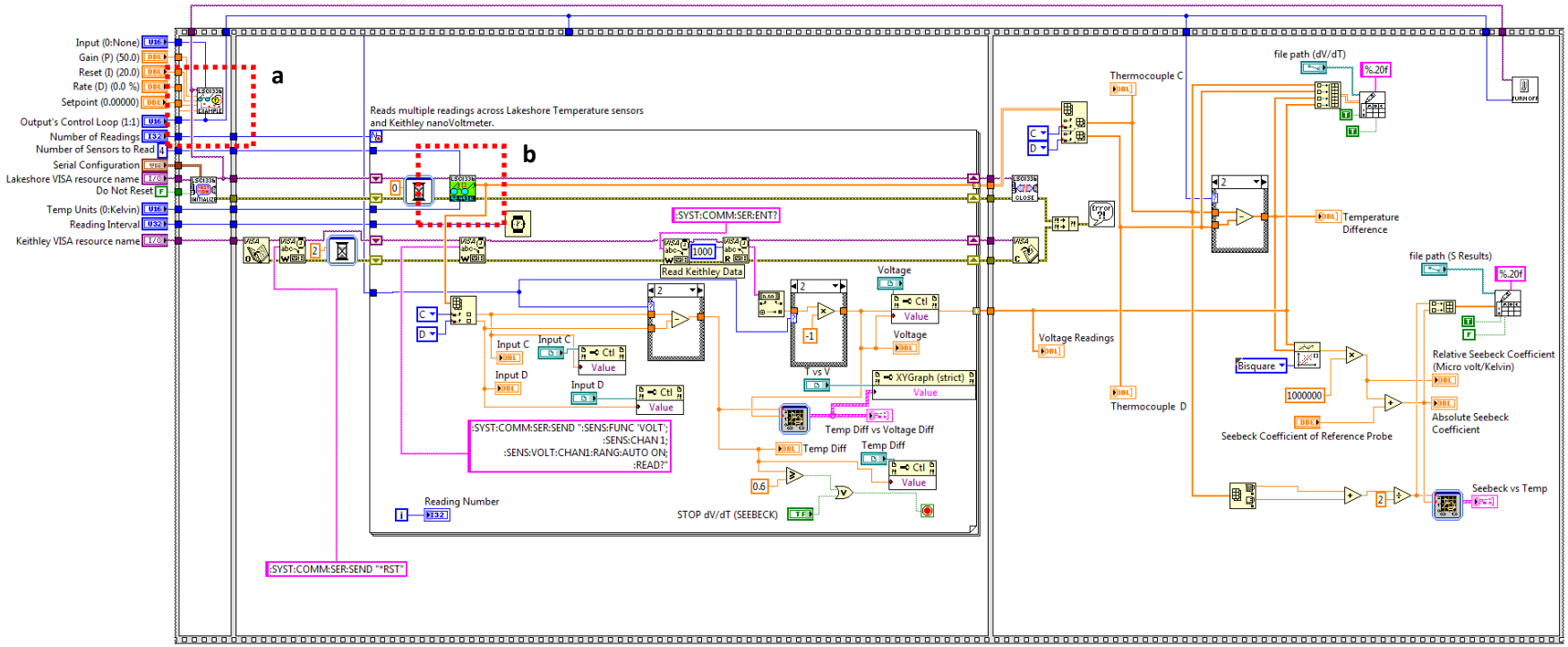

Figure 41. *SubVI for Seebeck coefficient measurement. Red boxes represent: (a) SubVI to configure heater parameters; (b) SubVI to read temperature data from 4 RTD sensors.*

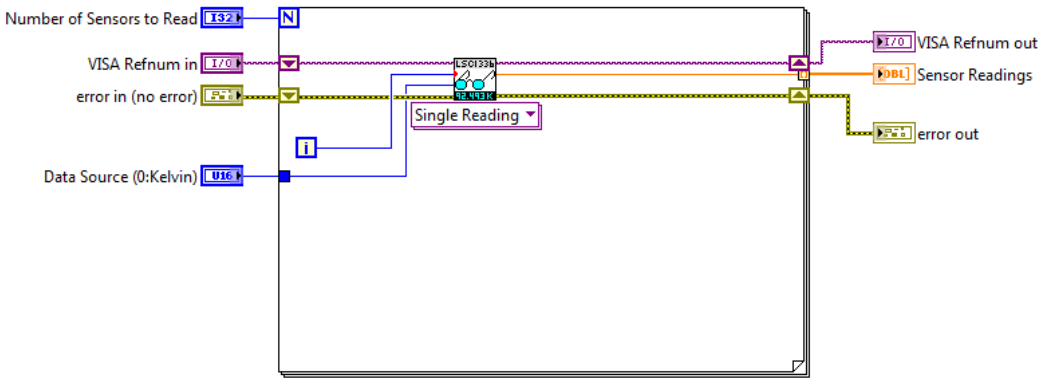

Figure 42. *SubVI to read temperature data from 4 RTD sensors.*

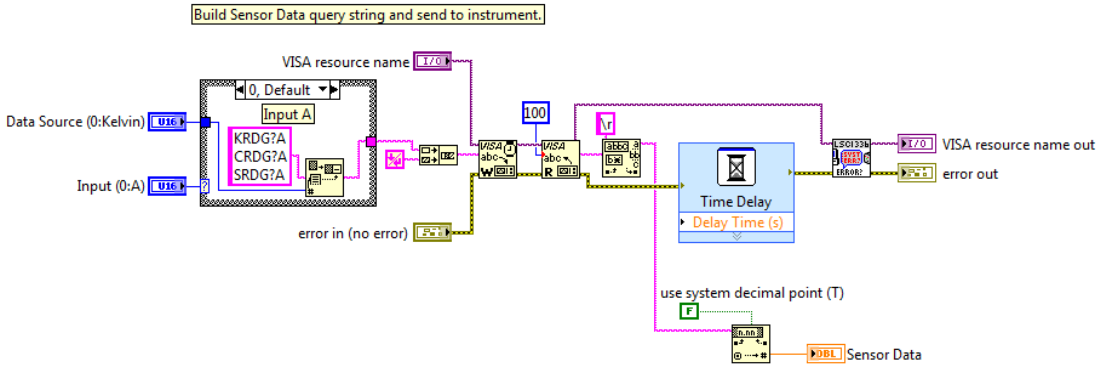

Figure 43. *SubVI to read data from single RTD sensor.*

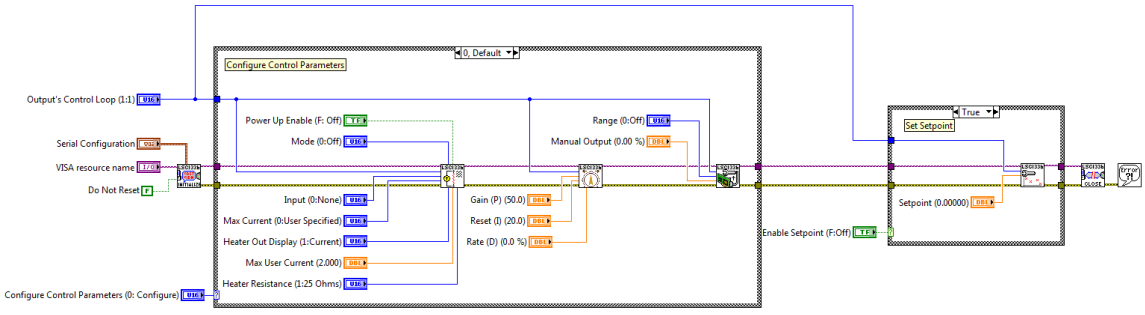

Figure 44. *SubVI to configure heater parameters.*

REFERENCES

1. Paul, D. Thermoelectric energy harvesting. *ICT-Energy-Concepts Towards Zero-Power Information and Communication Technology*. *InTech* 2014, 20, 21.

2. Soliman, E.; Al-Haik, M.; Taha, M. R. On and off-axis tension behavior of fiber reinforced polymer composites incorporating multi-walled carbon nanotubes. *Journal of Composite Materials* 2012, 46, 1661-1675.

3. Snyder, G. J.; Toberer, E. S. Complex thermoelectric materials. *Nat Mater* 2008, 7, 105-114.

4. Kim, G.; Shao, L.; Zhang, K.; Pipe, K. P. Engineered doping of organic semiconductors for enhanced thermoelectric efficiency. *Nature Materials* 2013, 12, 719-723.

5. Bubnova, O.; Khan, Z. U.; Malti, A.; Braun, S.; Fahlman, M.; Berggren, M.; Crispin, X. Optimization of the thermoelectric figure of merit in the conducting polymer poly (3, 4-ethylenedioxythiophene). *Nature Materials* 2011, 10, 429-433.

6. Yu, C.; Choi, K.; Yin, L.; Grunlan, J. C. Light-weight flexible carbon nanotube based organic composites with large thermoelectric power factors. *ACS nano* 2011, 5, 7885-7892.

7. Goldsmid, H. J. *Introduction to thermoelectricity*. Springer Science & Business Media: 2009; Vol. 121.

8. Cho, C.; Wallace, K. L.; Tzeng, P.; Hsu, J. H.; Yu, C.; Grunlan, J. C. Outstanding Low Temperature Thermoelectric Power Factor from Completely Organic Thin Films Enabled by Multidimensional Conjugated Nanomaterials. *Advanced Energy Materials* 2016.

9. Singh, R.; Bian, Z.; Shakouri, A.; Zeng, G.; Bahk, J.-H.; Bowers, J. E.; Zide, J. M.; Gossard, A. C. Direct measurement of thin-film thermoelectric figure of merit. *Applied Physics Letters* 2009, 94, 212508.

10. Mavrokefalos, A.; Pettes, M. T.; Zhou, F.; Shi, L. Four-probe measurements of the in-plane thermoelectric properties of nanofilms. *Review of scientific instruments* 2007, 78, 034901.

11. Singh, R.; Shakouri, A. Thermostat for high temperature and transient characterization of thin film thermoelectric materials. *Review of Scientific Instruments* 2009, 80, 025101.

12. Iwanaga, S.; Toberer, E. S.; LaLonde, A.; Snyder, G. J. A high temperature apparatus for measurement of the Seebeck coefficient. *Review of Scientific Instruments* 2011, 82, 063905.

13. Ponnambalam, V.; Lindsey, S.; Hickman, N.; Tritt, T. M. Sample probe to measure resistivity and thermopower in the temperature range of 300–1000K. *Review of scientific instruments* 2006, 77, 073904.

14. Zhou, Z.; Uher, C. Apparatus for Seebeck coefficient and electrical resistivity measurements of bulk thermoelectric materials at high temperature. *Review of Scientific Instruments* 2005, 76, 023901.

15. Boffoue, O.; Jacquot, A.; Dauscher, A.; Lenoir, B.; Stölzer, M. Experimental setup for the measurement of the electrical resistivity and thermopower of thin films and bulk materials. *Review of Scientific Instruments* 2005, 76, 3907.

16. Ravichandran, J.; Kardel, J.; Scullin, M.; Bahk, J.-H.; Heijmerikx, H.; Bowers, J.; Majumdar, A. An apparatus for simultaneous measurement of electrical conductivity and thermopower of thin films in the temperature range of 300–750 K. *Review of Scientific Instruments* 2011, 82, 015108.

17. Burkov, A.; Heinrich, A.; Konstantinov, P.; Nakama, T.; Yagasaki, K. Experimental set-up for thermopower and resistivity measurements at 100-1300 K. *Measurement Science and Technology* 2001, 12, 264.

18. Poumellec, B.; Marcelet, F.; Lagnel, F.; Marucco, J. Computer-controlled simultaneous measurements of the thermopower and conductivity of thin films. *Journal of Physics E: Scientific Instruments* 1988, 21, 159.

19. Beretta, D.; Bruno, P.; Lanzani, G.; Caironi, M. Reliable measurement of the Seebeck coefficient of organic and inorganic materials between 260 K and 460 K. *Review of Scientific Instruments* 2015, 86, 075104.

20. Cai, H.; Cui, D.; Li, Y.; Chen, X.; Zhang, L.; Sun, J. Apparatus for measuring the Seebeck coefficients of highly resistive organic semiconducting materials. *Review of Scientific Instruments* 2013, 84, 044703.

21. Pope, A.; Littleton IV, R.; Tritt, T. M. Apparatus for the rapid measurement of electrical transport properties for both “needle-like” and bulk materials. *Review of Scientific Instruments* 2001, 72, 3129-3131.

22. Yang, J. H.; Yip, H. L.; Jen, A. K. Y. Rational Design of Advanced Thermoelectric Materials. *Adv Energy Mater* 2013, 3, 549-565.

23. Zhao, W.; Fan, S.; Xiao, N.; Liu, D.; Tay, Y. Y.; Yu, C.; Sim, D.; Hng, H. H.; Zhang, Q.; Boey, F.; Ma, J.; Zhao, X.; Zhang, H.; Yan, Q. Flexible carbon nanotube papers with improved thermoelectric properties. *Energy & Environmental Science* 2012, 5, 5364.

24. Esfarjani, K.; Zebarjadi, M.; Kawazoe, Y. Thermoelectric properties of a nanocontact made of two-capped single-wall carbon nanotubes calculated within the tight-binding approximation. *Phys Rev B* 2006, 73.

25. Heremans, J. P.; Dresselhaus, M. S.; Bell, L. E.; Morelli, D. T. When thermoelectrics reached the nanoscale. *Nat Nanotechnol* 2013, 8, 471-473.

26. Yu, C.; Murali, A.; Choi, K.; Ryu, Y. Air-stable fabric thermoelectric modules made of N- and P-type carbon nanotubes. *Energy & Environmental Science* 2012, 5, 9481.

27. Moriarty, G. P.; Briggs, K.; Stevens, B.; Yu, C.; Grunlan, J. C. Fully Organic Nanocomposites with High Thermoelectric Power Factors by using a Dual-Stabilizer Preparation. *Energy Technology* 2013, 1, 265-272.

28. Kim, D.; Kim, Y.; Choi, K.; Grunlan, a. C.; Yu, C. Improved Thermoelectric Behavior of Nanotube-Filled Polymer Composites with Poly(3,4-ethylenedioxythiophene) Poly(styrenesulfonate). *ACS NANO* 2010, 4, 513–523.

29. Mai, C.-K.; Russ, B.; Fronk, S. L.; Hu, N.; Chan-Park, M. B.; Urban, J. J.; Segalman, R. A.; Chabinyc, M. L.; Bazan, G. C. Varying the ionic functionalities of conjugated polyelectrolytes leads to both p- and n-type carbon nanotube composites for flexible thermoelectrics. *Energy Environ. Sci.* 2015, 8, 2341-2346.

30. Nakai, Y.; Honda, K.; Yanagi, K.; Kataura, H.; Kato, T.; Yamamoto, T.; Maniwa, Y. Giant Seebeck coefficient in semiconducting single-wall carbon nanotube film. *Applied Physics Express* 2014, 7, 025103.

31. Burkov, A. *Thermoelectrics Handbook: Macro to Nano*. Boca Raton, FL: CRC: 2005.

32. Shakouri, A.; Li, S. In *Thermoelectric power factor for electrically conductive polymers*, Thermoelectrics, 1999. Eighteenth International Conference on, IEEE: 1999; pp 402-406.

33. Gripshover, R. J.; VanZytveld, J. B.; Bass, J. Thermopower of pure aluminum. *Physical Review* 1967, 163, 598.

34. Kasap, S. Thermoelectric effects in metals: thermocouples. *Canada: Department of Electrical Engineering University of Saskatchewan* 2001.

35. Moore, J.; Williams, R.; Graves, R. Precision measurements of the thermal conductivity, electrical resistivity, and Seebeck coefficient from 80 to 400 K and their application to pure molybdenum. *Review of Scientific Instruments* 1974, 45, 87-95.

36. Laubitz, M.; Matsumura, T.; Kelly, P. Transport properties of the ferromagnetic metals. II. Nickel. *Canadian Journal of Physics* 1976, 54, 92-102.

37. Desai, P. D.; James, H.; Ho, C. Y. Electrical resistivity of aluminum and manganese. *Journal of physical and chemical reference data* 1984, 13, 1131-1172.

38. Jordan, L.; Swanger, W. H. The properties of pure nickel. *Bureau of standards. J Res. doi* 1930, 10, 6028.

39. Desai, P. D.; Chu, T.; James, H. M.; Ho, C. Electrical resistivity of selected elements. *Journal of physical and chemical reference data* 1984, 13, 1069-1096.

40. Matula, R. A. Electrical resistivity of copper, gold, palladium, and silver. *Journal of Physical and Chemical Reference Data* 1979, 8, 1147-1298.

41. Cusack, N.; Kendall, P. The absolute scale of thermoelectric power at high temperature. *Proceedings of the physical society* 1958, 72, 898.

42. Gold, A.; MacDonald, D.; Pearson, W.; Templeton, I. The thermoelectric power of pure copper. *Philosophical Magazine* 1960, 5, 765-786.

43. MacDonald, D. K. C. *Thermoelectricity: an introduction to the principles*. Courier Corporation: 2006.

44. Roberts, R. The absolute scale of thermoelectricity II. *Philosophical Magazine B* 1981, 43, 1125-1135.

45. Blatt, J. *Thermoelectric power of metals*. Springer Science & Business Media: 2012.

46. White, G. K.; Woods, S. Electrical and thermal resistivity of the transition elements at low temperatures. *Philosophical Transactions of the Royal Society of London A: Mathematical, Physical and Engineering Sciences* 1959, 251, 273-302.

47. Blatt, F.; Flood, D.; Rowe, V.; Schroeder, P.; Cox, J. Magnon-drag thermopower in iron. *Physical Review Letters* 1967, 18, 395.

48. Heuer, H. W.; Wehrmann, R.; Kirchmeyer, S. Electrochromic window based on conducting poly (3,4-ethylenedioxythiophene)poly(styrene sulfonate). *Advanced Functional Materials* 2002, 12, 89-94.

49. Daoud, W. A.; Xin, J. H.; Szeto, Y. S. Polyethylenedioxythiophene coatings for humidity, temperature and strain sensing polyamide fibers. *Sensors and Actuators B-Chemical* 2005, 109, 329-333.

50. Andersson, P.; Nilsson, D.; Svensson, P. O.; Chen, M. X.; Malmstrom, A.; Remonen, T.; Kugler, T.; Berggren, M. Active matrix displays based on all-organic electrochemical smart pixels printed on paper. *Advanced Materials* 2002, 14, 1460-+.

51. Kim, G. H.; Shao, L.; Zhang, K.; Pipe, K. P. Engineered doping of organic semiconductors for enhanced thermoelectric efficiency. *Nature Materials* 2013, 12, 719-723.

52. Xia, Y.; Sun, K.; Ouyang, J. Solution-Processed Metallic Conducting Polymer Films as Transparent Electrode of Optoelectronic Devices. *Advanced Materials* 2012, 24, 2436-2440.

53. Ouyang, J.; Xu, Q. F.; Chu, C. W.; Yang, Y.; Li, G.; Shinar, J. On the mechanism of conductivity enhancement in poly (3,4-ethylenedioxythiophene): poly(styrene sulfonate) film through solvent treatment. *Polymer* 2004, 45, 8443-8450.

54. Dimitriev, O. P.; Grinko, D. A.; Noskov, Y. V.; Ogurtsov, N. A.; Pud, A. A. PEDOT:PSS films-Effect of organic solvent additives and annealing on the film conductivity. *Synthetic Metals* 2009, 159, 2237-2239.

55. Yeo, J. S.; Yun, J. M.; Kim, D. Y.; Kim, S. S.; Na, S. I. Successive solvent-treated PEDOT:PSS electrodes for flexible ITO-free organic photovoltaics. *Sol Energ Mat Sol C* 2013, 114, 104-109.

56. Deetuam, C.; Weise, D.; Samthong, C.; Praserthdam, P.; Baumann, R. R.; Somwangthanaroj, A. Electrical conductivity enhancement of spin-coated PEDOT:PSS thin film via dipping method in low concentration aqueous DMSO. *Journal of Applied Polymer Science* 2015, 132, 42108-42108.

57. Liu, S.; Deng, H.; Zhao, Y.; Ren, S.; Fu, Q. The optimization of thermoelectric properties in a PEDOT:PSS thin film through post-treatment. *Rsc Advances* 2015, 5, 1910-1917.

58. Ashizawa, S.; Horikawa, R.; Okuzaki, H. Effects of solvent on carrier transport in poly(3,4-ethylenedioxythiophene)/poly(4-styrenesulfonate). *Synthetic Metals* 2005, 153, 5-8.

59. Kim, J. Y.; Jung, J. H.; Lee, D. E.; Joo, J. Enhancement of electrical conductivity of poly(3,4-ethylenedioxythiophene)/poly(4-styrenesulfonate) by a change of solvents. *Synthetic Metals* 2002, 126, 311-316.

60. Jonsson, S. K. M.; Birgerson, J.; Crispin, X.; Greczynski, G.; Osikowicz, W.; van der Gon, A. W. D.; Salaneck, W. R.; Fahlman, M. The effects of solvents on the morphology and sheet resistance in poly (3,4-ethylenedioxythiophene)-polystyrenesulfonic acid (PEDOT-PSS) films. *Synthetic Met* 2003, 139, 1-10.

61. Kim, Y. H.; Sachse, C.; Machala, M. L.; May, C.; Muller-Meskamp, L.; Leo, K. Highly Conductive PEDOT:PSS Electrode with Optimized Solvent and Thermal Post-Treatment for ITO-Free Organic Solar Cells. *Advanced Functional Materials* 2011, 21, 1076-1081.

62. Okuzaki, H.; Harashina, Y.; Yan, H. Highly conductive PEDOT/PSS microfibers fabricated by wet-spinning and dip-treatment in ethylene glycol. *European Polymer Journal* 2009, 45, 256-261.

63. Sangeeth, C. S. S.; Jaiswal, M.; Menon, R. Correlation of morphology and charge transport in poly(3,4-ethylenedioxythiophene)-polystyrenesulfonic acid (PEDOT-PSS) films. *J Phys-Condens Mat* 2009, 21.

64. Bagchi, D.; Menon, R. Conformational modification of conducting polymer chains by solvents: Small-angle X-ray scattering study. *Chem Phys Lett* 2006, 425, 114-117.

65. Ouyang, L. Q.; Musumeci, C.; Jafari, M. J.; Ederth, T.; Inganas, O. Imaging the Phase Separation Between PEDOT and Polyelectrolytes During Processing of Highly Conductive PEDOT:PSS Films. *Acs Appl Mater Inter* 2015, 7, 19764-19773.